Title

Uncertainty Quantification of Hovering Rotor Noise Due to Gust-Induced Unsteady Loading Using Polynomial Chaos Expansion

Journal

Journal of the American Helicopter Society, 71(3)

ISSN

0002-8711

Authors

Gill, Hyunjune

Lee, Seongkyu

Publication Date

2026-07-01

DOI

10.4050/jahs.71.032001

Uncertainty Quantification of Hovering Rotor Noise Due to Gust-Induced Unsteady Loading Using Polynomial Chaos Expansion

Hyunjune Gill

PhD Candidate

Department of Mechanical and Aerospace Engineering

University of California

Davis, CA

Seongkyu Lee

Professor

Department of Mechanical and Aerospace Engineering

University of California

Davis, CA

Abstract

This study presents a polynomial chaos expansion (PCE)–based uncertainty quantification framework for predicting unsteady loading noise of a hovering rotor subjected to vertical gust disturbances. A sinusoidal gust model, characterized by gust amplitude and gust length, is introduced to represent realistic inflow variability arising from environmental effects or rotor–airframe interactions. Unsteady loading noise is predicted using a frequency-domain acoustic formulation coupled with two aerodynamic models: a quasi-steady blade element momentum theory and an indicial response method to capture aerodynamic memory effects. The PCE approach is employed to efficiently propagate gust-induced uncertainties through the aeroacoustic model and is systematically validated against Monte Carlo simulations, demonstrating excellent agreement while requiring substantially fewer model evaluations. The results show that the largest uncertainty in unsteady loading noise consistently occurs along the rotor axis, with uncertainty levels varying across blade-passing frequency harmonics. Gust length is found to be the dominant contributor to acoustic uncertainty at higher harmonics, whereas gust amplitude more strongly influences mid-harmonic noise levels. Incorporating unsteady aerodynamic effects reduces the mean sound pressure levels at all harmonics but does not significantly alter the overall uncertainty bounds. The proposed framework provides an efficient and physically interpretable tool for assessing rotor noise robustness under realistic inflow disturbances and supports the development of low-noise rotor designs for advanced air mobility applications.

Nomenclature

a Speed of sound, m/s

B Number of blades

C_l Coefficient of lift

C_{l_α} Lift-curve slope

C_n^c Circulatory lift

c Blade chord, m

c_{ij} PCE coefficients

c_{mB} Complex acoustic pressure, Pa

dT Sectional thrust, N

$\frac{dD}{dR}$ Drag per unit span, N/m

$\frac{dT}{dR}$ Thrust per unit span, N/m

F Prandtl's root and tip loss factor

He Hermite polynomial

l_g Gust length, m

M Freestream Mach number

m Acoustic harmonic index

R Blade section radius, m

R_t Rotor tip radius, m

r Normalized blade section radius

S Distance from rotor hub to an observer, m

s Distance traveled by airfoil in semi-chords

T_0 Gust onset time, s

t Time, s

U_P Local perpendicular velocity, m/s

U_T Local tangential velocity, m/s

V Freestream velocity, m/s

V_c Climb velocity or vertical gust velocity, m/s

V_p Amplitude of gust, m/s

V_{ref} Reference velocity, m/s

v_i Inflow velocity, m/s

Greek

α Angle of attack, rad

$\dot{\alpha}$ Pitch rate, rad/s

β Glauert factor, $\beta = \sqrt{1 - M^2}$

λ Loading harmonic index

λ_c Climb velocity ratio or vertical gust velocity ratio

λ_P Inflow ratio

Ω Rotation rate, rad/s

ϕ_n^c Indicial response function

Ψ Stochastic basis function

ψ Azimuthal angle, rad

ρ Air density, kg/m^3

σ Rotor solidity

θ Observer angle from the rotor axis, deg

θ_p Pitch angle, rad

ξ Random variable

Acronyms

BEMT Blade Element Momentum Theory

BPF Blade Passing Frequency

CV Coefficient of variation

eVTOL Electric Vertical Take-Off and Landing

MC Monte Carlo

PCE Polynomial Chaos Expansion

PCP Parallel Coordinate Plot

PDF Probability Density Function

SPL Sound Pressure Level

UAM Urban Air Mobility

UQ Uncertainty Quantification

Introduction

Rotorcraft and electric vertical takeoff and landing vehicles are playing a central role in the development of Advanced Air Mobility (AAM), which aims to enable on-demand air transportation in urban and suburban environments. The rapid progress in battery technology, electric propulsion systems, and distributed propulsion architectures has accelerated the deployment of AAM concepts in both commercial and government sectors. However, aeroacoustic performance remains a critical design driver, as community acceptance of AAM operations is largely dependent on aircraft noise [1]. Therefore, the development of effective noise-reduction technologies is critically important [2, 3, 4, 5].

In hovering or low-speed flight, rotor noise dominates the overall noise signature of many AAM aircraft, particularly at the blade-passing frequencies (BPFs) and their harmonics. While deterministic simulations have been widely used to model rotorcraft noise under nominal conditions [6, 7], realistic operating environments often involve uncertainties due to inflow disturbances, control system fluctuations, and environmental gusts [8, 9]. These unsteady and stochastic influences can lead to significant variations in acoustic signatures. As such, uncertainty quantification (UQ) is essential for designing robust rotor systems and ensuring compliance with community noise requirements.

Recent studies have demonstrated the sensitivity of rotor noise to variations in inflow and operational parameters. For instance, Li et al. [10] found that small periodic fluctuations in rotor RPM—common in feedback-controlled eVTOL systems—can induce additional tonal components in the acoustic spectrum. Similarly, vertical gusts have been shown to modulate unsteady loading, altering both the magnitude and spectral content of radiated noise [11, 12, 13]. Despite this, most aeroacoustic models are built on deterministic inputs, with limited integration of UQ frameworks.

To address this gap, polynomial chaos expansion (PCE) can be used as a powerful method for propagating input uncertainties through nonlinear aerodynamic or acoustic models. PCE offers faster convergence and reduced computational cost compared to traditional Monte Carlo (MC) simulations, particularly for problems with low to moderate stochastic dimensionality [14, 15]. Prior applications of PCE in aeroacoustics have shown its effectiveness in capturing uncertainty in tonal or broadband noise due to variability in flow conditions, geometry, and boundary-layer properties [16].

This study employs PCE-based UQ to analyze the unsteady loading noise from a hovering rotor subjected to vertical gusts. Vertical gusts can arise from atmospheric pressure fluctuations or be induced by nearby structures. For instance, Fig.1 illustrates a potential mechanism for the generation of vertical gusts acting on a rotor. A typical drone or AAM aircraft configuration [17, 18] places a strut or wing directly beneath the rotor during hover. As the rotor blades sweep over such structures, disturbances in vertical velocity can develop due to rotor-body interaction. These localized variations in inflow velocity modify the aerodynamic loading on the blades and can serve as a source of unsteady loading noise.

A sinusoidal gust model, characterized by gust amplitude and wavelength, is introduced. The sinusoidal gust representation provides a mathematically tractable and physically interpretable form that isolates the essential mechanisms associated with periodic inflow disturbances. This approach allows us to systematically examine parameter sensitivities, frequency-dependent loading, and the resulting acoustic response in a controlled manner. Two aerodynamic models are used and compared: a quasi-steady blade element momentum theory (BEMT) and BEMT augmented with the indicial response method [19].

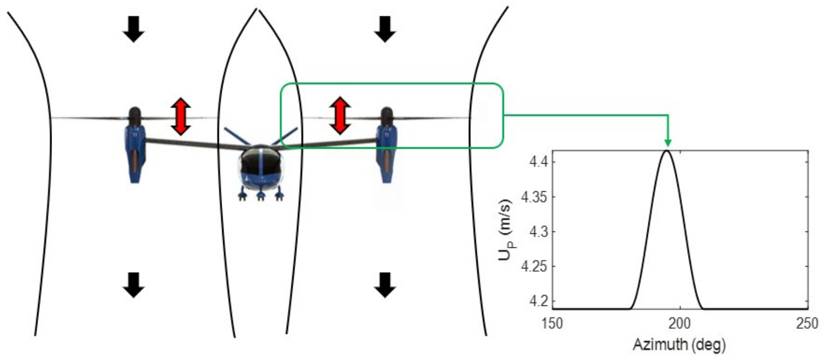

Fig. 1: Rotor and wing interactions, causing the vertical gust on the rotor blades.

The indicial method is particularly useful for fully accounting for unsteady effects, as it retains the memory of the unsteady loading history. Since the present study focuses on rapid UQ analyses, aerodynamic simulations are carried out using BEMT combined with the indicial response method instead of more time-consuming simulations like the panel method, free-wake or CFD solvers. For aeroacoustic prediction, the unsteady loading noise model developed by Goldstein [20] is employed. This frequency-domain approach enables rapid and efficient computation of far-field noise.

The goal is to quantify not only the mean acoustic response, but also the uncertainty bounds arising from variations in gust characteristics. The results are validated against MC simulations, and visual tools such as parallel coordinate plots are employed to identify parameter combinations leading to noise outliers. Additionally, the resulting noise uncertainties from the two aerodynamic approaches—with and without the indicial response method—are compared to highlight the acoustic impact of unsteady aerodynamic effects. This work builds upon and extends recent efforts to integrate UQ into rotorcraft noise modeling, and contributes to the ongoing development of quiet design of AAM vehicles [21, 22].

Methodology

Aerodynamic Model

In the case of a hovering rotor, classical methods such as BEMT provide only steady aerodynamic loads across the rotor disk, as they assume a uniform distribution of inflow velocity along the azimuth. While this assumption is adequate for rotor performance analysis, it limits the capability to accurately predict acoustic characteristics in realistic hovering conditions. Traditional frequency-domain methods [23, 24, 25, 26, 27, 20, 28] have shown that tonal noise is theoretically absent along the rotor axis during hover or axial forward flight. However, experimental observations [11, 29, 30] consistently indicate the presence of significant tonal noise along the rotor axis, which has been attributed to unsteady inflow conditions.

To reconcile these discrepancies, Gill and Lee [12] employed a quasi-steady extension of BEMT that incorporates unsteady parameters, such as variations in rotational speed or vertical gusts. These parameters are allowed to vary both radially and azimuthally across the rotor disk, enabling a more realistic representation of unsteady inflow conditions.

The sectional thrust from blade element theory is given by:

$$dT = \frac{B}{2\pi}\int_0^{2\pi} \frac{1}{2}\rho U_T^2 c C_l \, dR \, d\psi \tag{1}$$

where B is the number of blades, ρ is the air density, U_T is the local tangential velocity, c is the chord length, C_l is the lift coefficient, dR is the differential radial element, and $d\psi$ is the differential azimuthal angle in radians. The sectional thrust from momentum theory, without assuming a uniform inflow distribution, is given by:

$$dT = \int_0^{2\pi} 2\rho(V_c + v_i)v_i R \, dR \, d\psi \tag{2}$$

where V_c is, by definition, the climb or axial velocity at the rotor disk; however, the present study utilizes V_c to model vertical gust, and a method of modeling vertical gust is discussed later in this subsection. v_i is the inflow velocity. By equating Eq. (1) and Eq. (2), the local perpendicular velocity (U_P) at any given location on the rotor disk can be derived as follows:

$$U_P(R,\psi) = \sqrt{\left(\frac{BcC_{l\alpha}U_T(R,\psi)}{16\pi FR} - \frac{V_c(R,\psi)}{2}\right)^2 + \frac{BcC_{l\alpha}\theta_p U_T(R,\psi)^2}{8\pi FR}} - \left(\frac{BcC_{l\alpha}U_T(R,\psi)}{16\pi FR} - \frac{V_c(R,\psi)}{2}\right) \tag{3}$$

where $U_P = (V_c + v_i)$. U_T and U_P are now functions of the blade radius (R) and the azimuth angle (ψ). $C_{l\alpha}$ is the lift-curve slope, F is Prandtl's tip and root loss function, and θ_p is the blade pitch angle. The non-dimensional form of Eq. (3) can be obtained by dividing both sides of the equation by ΩR_t, where R_t is the rotor radius. The resulting non-dimensional form for a rotor with rectangular blades is shown in

Table 1: Constants of the indicial response function ($\phi_n^c(s)$).

$\phi_n^c(s) = 1 - A_1 e^{-b_1 s} - A_2 e^{-b_2 s}$			
A_1	A_2	b_1	b_2
0.165	0.335	0.0455	0.3

Eq. (4) below:

$$\lambda_P(r,\psi,\lambda_c) = \sqrt{\left(\frac{\sigma C_{l_\alpha}}{16F} - \frac{\lambda_c}{2}\right)^2 + \frac{\sigma C_{l_\alpha}}{8F}\theta_p r} - \left(\frac{\sigma C_{l_\alpha}}{16F} - \frac{\lambda_c}{2}\right) \tag{4}$$

where $\lambda_P = \frac{U_P}{\Omega R_t}$, $\lambda_c = \frac{V_c}{\Omega R_t}$, and $\sigma = \frac{Bc}{\pi R_t}$ for a rectangular-bladed rotor. This form is identical to the steady-state BEMT inflow ratio formulation [31], thus indicating that the aerodynamic loads are determined using the quasi-steady approach [12]. However, this approach neglects the amplitude change and phase shift due to the unsteady aerodynamics. To fully include the unsteady aerodynamic effects, the indicial method proposed by Wagner [32] is incorporated into the quasi-steady BEMT. The indicial method introduces a correction to the lift coefficient in response to an arbitrary variation in angle of attack. The proposed unsteady aerodynamic model is as follows:

$$C_l^c(t) = 2\pi\left(\alpha(0)\phi(s) + \int_0^s \frac{d\alpha(\eta)}{dt}\phi(s-\eta)d\eta\right) = 2\pi\alpha_e(t) \tag{5}$$

where $C_l^c(t)$ is the circulatory lift coefficient, t is the temporal step in the azimuth or $t = \psi/\Omega$, $\phi(s)$ is Wagner's response function as defined in Table 1, s is the distance traveled by airfoil in semi-chords, and η is a dummy variable for Duhamel integration. The indicial lift response is useful in the development of a general time domain unsteady aerodynamic theory for rotor analyses. The unsteady loads with respect to arbitrary changes in angle of attack can be determined through the superposition of indicial aerodynamic responses using the Duhamel integral if the indicial response is known.

For the quasi-steady approach, a local thrust can be calculated using the following expression:

$$dT(R,\psi) = \frac{B}{4\pi}\rho U_T(R,\psi)^2 c C_{l\alpha}(\theta_p - \phi(R,\psi))dR \tag{6}$$

where $\phi(R,\psi)$ is the inflow angle. One of the advantages of this approach is that the tangential and vertical velocities can be modeled mathematically for simplicity or measured directly through experiments. Note that the $C_{l\alpha}(\theta_p - \phi(R,\psi))$ term equals the lift coefficient C_l at the corresponding R and ψ locations.

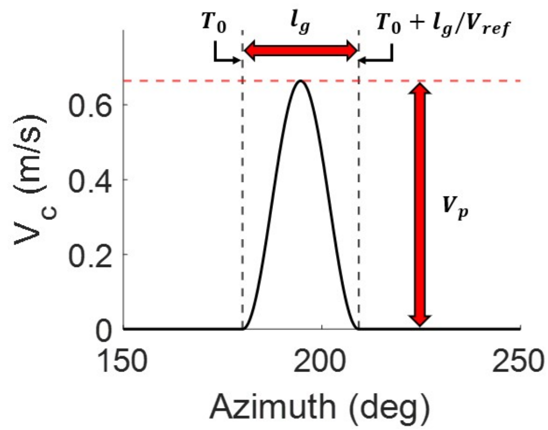

Fig. 2: An example gust modeled by Eq. (7).

To incorporate the unsteady aerodynamic effect using the indicial response method, this term is replaced by $C_l^c(t)$ from Eq. (5), and α in Eq. (5) is determined from the quasi-steady solutions $(\theta_p - \phi(R, \psi))$. The effect of unsteady aerodynamics will be compared with the quasi-steady approach in the uncertainty quantification analyses.

The present study considers the effect of the vertical gust on the unsteady loading noise. A gust modeling method as shown in Eq. (7) is adopted from Wang et al. [33]

$$V_c(t) = \begin{cases} \frac{1}{2} V_p \left(1 - \cos\left(\frac{2\pi(t-T_0)V_{\text{ref}}}{l_g}\right)\right) & T_0 < t < T_0 + l_g/V_{\text{ref}}, \\ 0 & \text{otherwise}, \end{cases} \tag{7}$$

where l_g is the gust length, V_p is the peak gust velocity, V_{ref} is a reference velocity obtained from 70% of the blade radius, T_0 is the time of gust onset, $t = \psi/\Omega$, and Ω is the rotation rate in radians per second. The resulting vertical velocity V_c in Eq. (7) is used as the climb velocity V_c in Eq. (2) at a given time or azimuthal location.

Figure 2 shows an example of the modeled gust that a section of one blade experiences during its revolution. The black dashed lines indicate the onset (T_0) and end of the vertical gust in time, the distance between these dashed lines defines the gust length (l_g), and the red dashed line indicates the amplitude of the vertical gust (V_p). Since the shape and size of the gust can be mainly characterized by the gust length and amplitude, uncertainty quantification is carried out using these two parameters.

As a test problem, the vertical gust is modeled with $l_g = 0.125$ m, $T_0 = 0.02$ s, and $V_p = 0.6641$ m/s at all radial locations at an onset azimuth angle corresponding to $T_0 = 0.02$ s. The test case is chosen based on the experimental configuration reported by Kvurt and Stalnov [11], with the operating conditions summarized in Table 2. Figures 3(a) and 3(b) show the perpendicular velocity (U_P) and the corresponding thrust distribution on the rotor disk obtained from quasi-steady BEMT after incorporating the modeled vertical gust. The black circles on the contour plots indicate the 70% spanwise location of the rotor radius, where the sectional thrust reaches its maximum. This location is also where the thrust values are extracted for further analysis, as illustrated in Fig. 3(c). Introducing a vertical gust near the 200° azimuth increases the magnitude of the perpendicular velocity across the rotor disk, resulting in a local reduction in the angle of attack. This decrease in angle of attack, in turn, leads to a reduction in thrust at that location in the quasi-steady BEMT model. However, when unsteady aerodynamic effects are included via the indicial response method, both a phase shift and a change in the amplitude of the thrust fluctuation are observed. As shown by the red line in Fig. 3(c), the unsteady aerodynamic model predicts a smaller reduction in thrust, and the location of minimum thrust shifts aft of the location of the minimum thrust from the quasi-steady model. It also shows a gradual increase in thrust downstream of the minimum. This effect of the unsteady aerodynamic model on thrust magnitude and phase shift agrees with the findings presented by Arnhem et al. [34], in which they compared the thrust distribution predicted by the full-blade CFD with that by the quasi-steady and unsteady models.

Table 2: Operating condition of Mejzlik heavy duty (HD) rotor [11].

B	Radius (m)	RPM	Obs. Distance (m)
3	0.3556	1500	1.5

Aeroacoustic Model

Goldstein's frequency-domain tonal noise model [20] is selected to analyze the unsteady loading noise of a hovering rotor due to its ability to rapidly predict loading noise in the presence of unsteady inflow distributions. Without delving into the detailed derivations, the final formulation of the model is provided

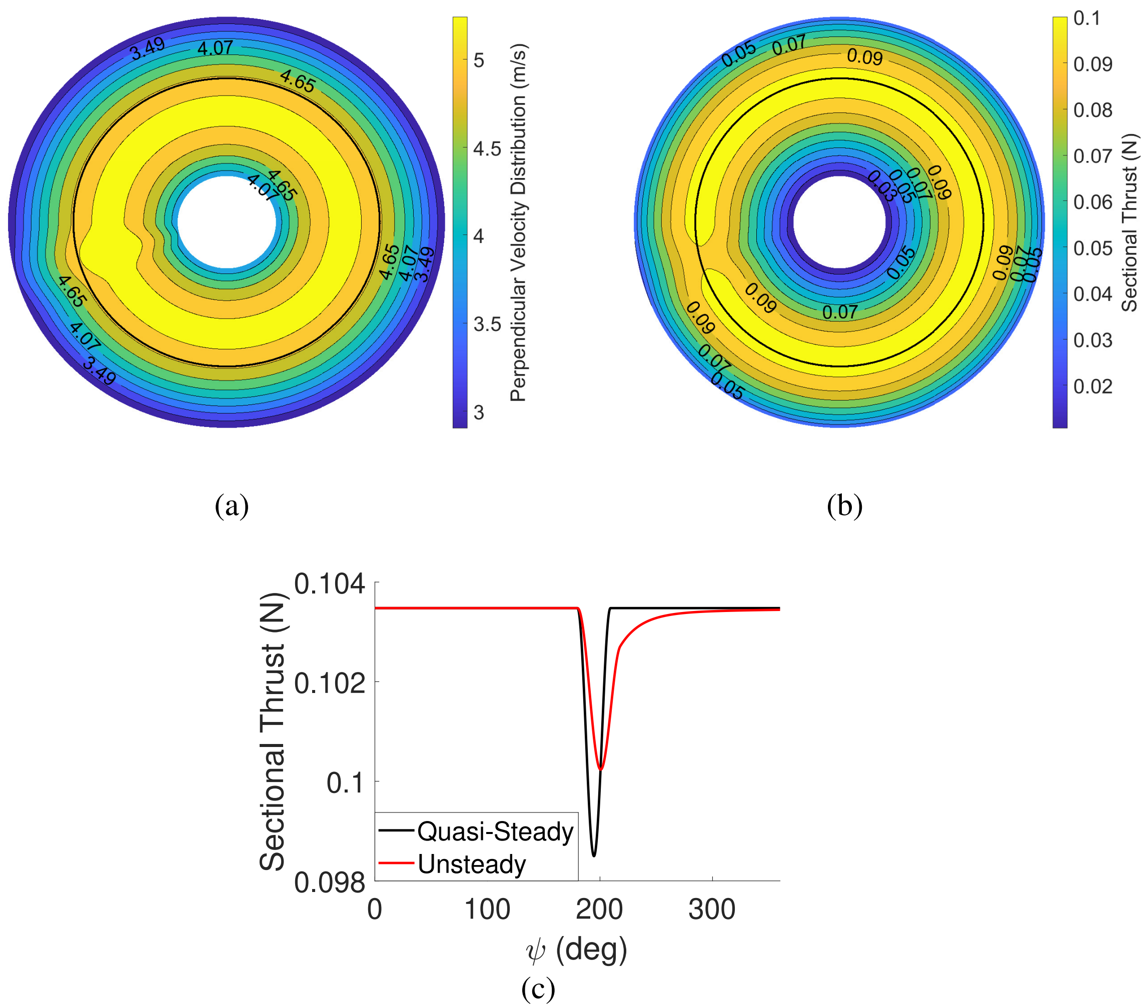

Fig. 3: Mejzlik rotor test problem with a vertical gust: (a) perpendicular velocity distribution on the rotor disk, (b) thrust distribution on the rotor disk, and (c) sectional thrust at 70% of the rotor disk.

as follows:

$$c_{mB} = \frac{imB^2\Omega}{4\pi aS} e^{i\frac{mB\Omega S}{a}} \sum_{\lambda=-\infty}^{\infty} e^{i(mB-\lambda)(\psi'-\pi/2)} \int_{hub}^{tip} \left[\cos\theta \frac{dT}{dR}\Big|_{\lambda} - \frac{a(mB-\lambda)}{mB\Omega R} \frac{dD}{dR}\Big|_{\lambda} \right] \times J_{mB-\lambda} \left(\frac{mB\Omega R}{a} \sin\theta \right) dR \tag{8}$$

where m is the acoustic harmonic index, λ is the loading harmonic index, Ω is the rotation rate in radians per second, S is the observer distance from the rotor hub, $\psi' = \cos^{-1}(z/Y)$ is the in-plane observer angle, and θ is the observer angle from the rotor axis. Figure 4 illustrates the coordinate system used for rotor orientation and observer location in the acoustic analysis. The key aerodynamic inputs from the aerodynamic solvers are $\frac{dT}{dR}\big|_{\lambda}$ (sectional thrust per unit span) and $\frac{dD}{dR}\big|_{\lambda}$ (sectional drag per unit span). These inputs are the aerodynamic loads on a single blade. To account for the loads of a rotor with multiple identical blades, an additional B has been multiplied in Eq. (8). The temporal history of loads at each radial section, computed from the modified BEMT or the indicial method, is transformed into the frequency domain using a Fourier series, given by:

$$\frac{dT(R,\psi)}{dR} = \sum_{\lambda=-\infty}^{\infty} \frac{dT}{dR}\Big|_{\lambda} e^{i\lambda\psi} \tag{9}$$

It is important to note that a compact source assumption is made in this version of Goldstein's model. In the original model, chordwise non-compactness was considered in the aerodynamic load inputs to account for the retarded time variation between the blade surfaces and the rotational plane of the propeller. However, neither the modified BEMT nor the indicial method considers the chordwise variation of the aerodynamic loads. Thus, the chordwise non-compactness effect is neglected.

The acoustic pressure in Eq. (8) is then converted to sound pressure level (SPL) using the following expression:

$$\text{SPL} = 20\log_{10}\frac{|P_{\text{rms}}|}{P_{\text{ref}}} \tag{10}$$

where P_{rms} is the root mean square pressure of the single-sided noise spectrum, and P_{ref} is the reference pressure, taken as 20μPa. The root mean square pressure is obtained by dividing c_{mB} by $\sqrt{2}$.

Uncertainty Quantification Analysis: Polynomial Chaos Expansion (PCE)

PCE is a mathematical method used in UQ to efficiently model how uncertainties in input parameters propagate through a system and affect its outputs. For instance, the probability density function (PDF)

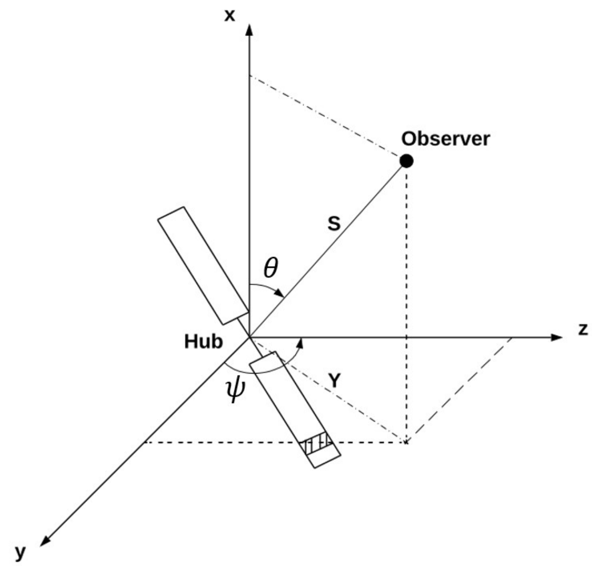

Fig. 4: Coordinate system used for the acoustic analysis.

of the input parameters can be approximated using Eq. (11), where $\boldsymbol{X}$ represents the input uncertainty parameters, such as the vertical gust amplitude or length. In this formulation, c_i represents the coefficient, and Ψ_i is the stochastic basis function (polynomials).

$$\boldsymbol{X} \approx \sum_{i=0}^{p} c_i \Psi_i(\boldsymbol{\xi}), \quad \boldsymbol{X} : \{V_p, l_g\} \tag{11}$$

where p is the order of polynomial truncation and $\boldsymbol{\xi}$ is a vector of the random variables between 0 and 1 for each input parameter. If the basis function, Ψ_i, is known, the coefficients can be determined using the definition provided in Eq. (12), which is a general form of PCE for any single input parameters X.

$$\begin{aligned} c_i &= \frac{1}{\Psi_i^2} \int_{\Omega} X \Psi_i(\xi) \rho(\xi) d\xi \\ \Psi_i^2 &= \frac{\int \chi(\xi) \Psi(\xi) \rho(\xi) d\xi}{\int \rho(\xi) \Psi^2(\xi) d\xi} \end{aligned} \tag{12}$$

where ρ is the PDF of the random variable and $\chi(\xi)$ is the transformed random variable of ξ to reflect the physical space of the input parameter. For instance, if the random variable is normally distributed (N) with a mean of 0 and standard deviation of 1, the random variable and the transformed random variable

Table 3: Range of input uncertainty parameters.

Input Uncertainty Parameters	Range
Peak Gust Amplitude (V_p)	0.266 – 1.063 m/s
Gust Length (l_g)	0.05 m – 0.2 m

can be represented as

$$\begin{aligned} &\xi \sim N(0,1) \quad \text{with} \quad \rho(\xi) = \frac{1}{\sqrt{2\pi}} e^{-\frac{\xi^2}{2}} \\ &\chi(\xi) \sim N(M_N, S_N) \\ &\chi(\xi) = S_N \xi + M_N \end{aligned} \tag{13}$$

where M_N and S_N are mean and standard deviation of the input variable, which are prescribed by the user. The ranges of the input uncertainty parameters are summarized in Table 3, where the mean values are selected to represent realistic operating conditions. These ranges are chosen based on the feasibility of gust strength and spatial extent that could plausibly occur in experimental environments or during in-flight operations. For example, the peak gust amplitude is specified to range from 0.266 to 1.063 m/s, corresponding to 5% to 20% of the induced velocity under steady-state conditions. The gust length is assumed to vary between 0.05 and 0.2 m, which is approximately equivalent to 10 to 40 degrees of rotor azimuth. The mean values of the uncertainty parameters are taken as the median of these respective ranges. To quantify the associated uncertainty, the standard deviation is determined using the coefficient of variation (CV), defined as CV $= S_N/M_N$.

The stochastic basis functions used in PCE framework are selected based on the probability distribution of the input random variables, as summarized in Table 4. Each type of distribution is associated with a corresponding set of orthogonal polynomials. In the present study, the uncertain input parameters are assumed to follow a Gaussian (normal) distribution. Accordingly, the Hermite polynomials are chosen as the appropriate stochastic basis functions. The Hermite polynomial of order i is defined by Eq. (14).

$$\Psi_i(\xi) = \mathrm{He}_i(\xi) = (-1)^i e^{\frac{\xi^2}{2}} \frac{d^i}{d\xi^i} e^{\frac{-\xi^2}{2}} \tag{14}$$

Table 4: Distribution type of input random variables and the corresponding orthogonal polynomials.

Uncertain Parameter Type	Orthogonal Polynomials
Gaussian	Hermite
Gamma	Laguerre
Beta	Jacobi
Uniform	Legendre

A general form of PCE is as follows:

$$Y(\xi_1, \xi_2, ..., \xi_d) = \sum_{i \in \mathbb{I}_p} c_i \Psi_i(\xi_1, \xi_2, ..., \xi_d) \tag{15}$$

where Y is the output quantity of interest, ξ_d denotes the input random variables, c_i is the PCE coefficient associated with the multi-index i, and Ψ_i represents the multivariate stochastic basis functions, which are Hermite polynomials in the present study due to the assumption of Gaussian-distributed inputs. The index i belongs to the index set $\mathbb{I}_p$, which includes all admissible multi-indices satisfying the total-degree truncation condition up to order p. For instance, when $p = 2$ and there are two input variables (ξ_1 and ξ_2), the general expansion in Eq. (15) includes all terms such that the total polynomial degree $i_1 + i_2 \leq 2$, and can be explicitly written as:

$$\begin{aligned} Y(\xi_1, \xi_2) = & c_{(0,0)}\Psi_{(0,0)} + c_{(1,0)}\Psi_{(1,0)} + c_{(0,1)}\Psi_{(0,1)} \\ & + c_{(2,0)}\Psi_{(2,0)} + c_{(1,1)}\Psi_{(1,1)} + c_{(0,2)}\Psi_{(0,2)}. \end{aligned} \tag{16}$$

or simply

$$Y(\xi_1, \xi_2) = \sum_{i+j=0}^{p=2} c_{ij} \Psi_i(\xi_1) \Psi_j(\xi_2) \tag{17}$$

where the summation of indices, i and j, do not exceed $p = 2$. The total number of terms in the expansion can be determined by Eq. (18).

$$N = \frac{(p+d)!}{p!d!} \tag{18}$$

where d denotes the number of variables.

Since a third-degree truncation has been found sufficient to obtain a converged solution, a two-variable PCE with third-degree truncation, as represented by Eq. (19), is employed to quantify the uncertainty in the SPL arising from the variability in the gust parameters.

$$
\begin{aligned}
\mathrm{SPL}(\xi_1, \xi_2) &= \sum_{i+j=0}^{p=3} c_{ij} \Psi_i(\xi_1) \Psi_j(\xi_2) \\
&= c_{00}(1) + c_{10}(\xi_1) + c_{01}(\xi_2) + c_{11}(\xi_1)(\xi_2) \\
&+ c_{20}(\xi_1^2 - 1) + c_{02}(\xi_2^2 - 1) + c_{21}(\xi_1^2 - 1)(\xi_2) \\
&+ c_{12}(\xi_1)(\xi_2^2 - 1) + c_{30}(\xi_1^3 - 3\xi_1) + c_{03}(\xi_2^3 - 3\xi_2)
\end{aligned} \tag{19}
$$

Following Eq. (18), there is a total number of 10 terms in the expansion of the third-degree truncated two variable PCE, as shown in Eq. (19).

The roots of the orthogonal polynomial of one order higher than the degree of truncation, along with zero, are chosen as the collocation points at which the actual output SPLs are evaluated. For instance, since a third-degree truncation is adopted, the roots of the fourth-order Hermite polynomial, including zero, are selected for each input variable. These roots are given by $\{-1.65, -0.52, 0, 0.52, 1.65\}$. The tensor product of these collocation points for two input random variables results in the combinations shown in Table 5. Consequently, a total of 25 simulations are required to quantify the uncertainty in SPL, yielding a 25×10 matrix used to determine the PCE coefficients. Equation (20) presents the matrix form relating the output SPLs to the corresponding basis functions and the coefficients. Each row of this 25×10 matrix represents the evaluations of the Hermite polynomials at a given collocation point, while each column corresponds to a particular polynomial basis function formed from the combinations of the two random variables. The PCE coefficients are then determined by solving Eq. (20), using the SPL values obtained from the 25 simulations.

$$
\begin{bmatrix} \mathrm{SPL}_1 \\ \mathrm{SPL}_2 \\ \vdots \\ \mathrm{SPL}_{24} \\ \mathrm{SPL}_{25} \end{bmatrix} = \begin{bmatrix} 1 \; \xi_1 \; \xi_2 \cdots (\xi_1^3 - 3\xi_1) \; (\xi_2^3 - 3\xi_2) \\ 1 \; \xi_1 \; \xi_2 \cdots (\xi_1^3 - 3\xi_1) \; (\xi_2^3 - 3\xi_2) \\ \vdots \qquad \cdots \qquad \vdots \\ 1 \; \xi_1 \; \xi_2 \cdots (\xi_1^3 - 3\xi_1) \; (\xi_2^3 - 3\xi_2) \\ 1 \; \xi_1 \; \xi_2 \cdots (\xi_1^3 - 3\xi_1) \; (\xi_2^3 - 3\xi_2) \end{bmatrix} \begin{bmatrix} c_{00} \\ c_{10} \\ \vdots \\ c_{30} \\ c_{03} \end{bmatrix} \tag{20}
$$

Once the PCE coefficients are determined from Eq. (20), any combination of the two random variables,

Table 5: Combination of all collocation points to determine PCE output coefficients.

Simulation Counts	ξ_1	ξ_2
1	-1.65	-1.65
2	-1.65	-0.52
⋮	⋮	⋮
5	-1.65	1.65
6	-0.52	-1.65
7	-0.52	-0.52
⋮	⋮	⋮
24	1.65	0.52
25	1.65	1.65

assumed to follow a normal distribution as shown in Eq. (13), can be substituted into Eq. (19) to evaluate the corresponding output SPL. This approach allows for a significant reduction in the number of aerodynamic and aeroacoustic simulations required to quantify acoustic uncertainties compared to the traditional MC method. It is important to note that the output SPL computed from Eq. (19) corresponds to a single observer location and a specific acoustic harmonic index. Therefore, if multiple acoustic harmonics or various observer locations are of interest, the PCE procedure must be repeated to obtain separate sets of PCE coefficients corresponding to each harmonic index or observer position.

Uncertainty Quantification Analysis: Monte Carlo (MC)

Compared to the PCE method, the MC method requires executing both aerodynamic and aeroacoustic solvers for a large number of sampled input parameters to evaluate the corresponding SPLs. A schematic representation of the MC simulation procedure is shown in Fig. 5. Based on the specified mean and standard deviation of the input parameters, a set of normally distributed random variables is generated and used in the aerodynamic solver to compute the unsteady aerodynamic loads on the rotor disk. These loads are then input to the acoustic solver to determine the corresponding SPLs due to unsteady loading noise. For the single-variable uncertainty quantification cases, 50 MC iterations are performed for converged solutions, while 400 iterations are performed for the two-variable MC simulations. As the MC method requires explicit evaluations of the output for every sample of the uncertain input parameters, it can be computationally expensive and time-consuming, especially when high-fidelity aerodynamic and acoustic solvers are employed.

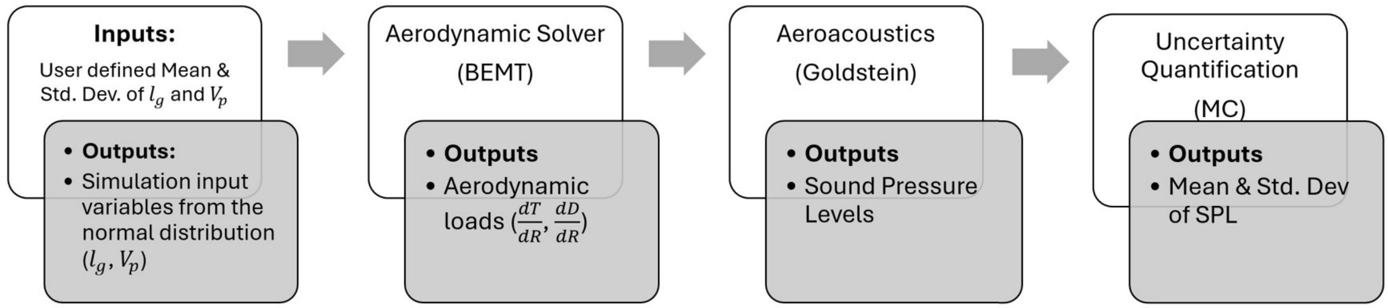

Fig. 5: Schematic of Monte Carlo simulation.

Results

In this section, the PCE method is first validated against the MC method. Following this validation, UQ results are presented for three representative cases: (1) acoustic impact due to gust length alone, (2) acoustic impact due to gust amplitude alone, and (3) acoustic impact due to the combined variation of gust length and amplitude. For each case, the unsteady loading noise is evaluated using two aerodynamic models: one that incorporates unsteady aerodynamic effects through the indicial response method and another based on the quasi-steady formulation. This comparative analysis elucidates the role of unsteady aerodynamic effects in shaping acoustic uncertainty. As the primary objective of this study is to quantify the uncertainty in unsteady loading noise arising from variability in gust parameters, direct comparisons with experimental measurements are not included.

Validation of PCE

Figure 6 presents the noise directivity patterns for the first five BPF harmonics, illustrating the uncertainty introduced by variations in gust amplitude (V_p). Although higher-harmonic noise is present, our analysis confirms that the noise variability decays beyond the 5^{th} harmonic, as demonstrated in the Appendix, where the uncertainty quantification is presented up to the 15^{th} harmonic. Therefore, for the sake of brevity and clarity, we have chosen to report results only up to the 5^{th} harmonic in this paper. Here, $\theta = 0^\circ$ and 180° correspond to the rotor axis, while $\theta = 90^\circ$ denotes the rotor plane. The mean SPLs predicted using the MC method (black solid line) are compared with those obtained from the PCE method (red dashed line). The close agreement between the two predictions demonstrates that the PCE method reliably captures the mean acoustic trends obtained from the MC method while requiring substantially

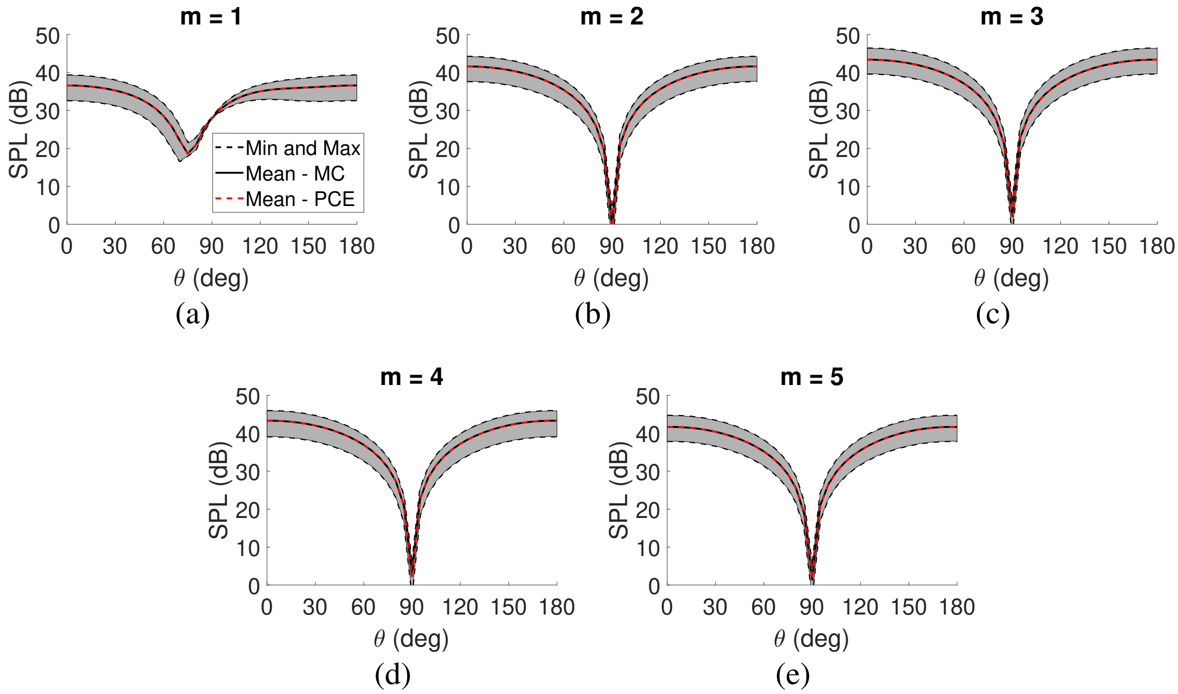

Fig. 6: Distribution of unsteady loading noise due to variations in gust amplitude (V_p) at various observer locations (CV = 0.1): (a) 1st BPF noise, (b) 2nd BPF noise, (c) 3rd BPF noise, (d) 4th BPF noise, and (e) 5th BPF noise.

fewer simulations. Similar consistency has been observed in other cases, including uncertainty due to gust length alone and combined variations in gust parameters [35].

Acoustic Impact due to Gust Length Alone

One characteristic of a gust that can induce unsteadiness in aerodynamic loads on a rotor disk is its length. The gust amplitude is kept constant at its mean while performing UQ analyses with respect to gust length. Figure 7 shows the uncertainty of SPLs at multiple BPFs across various observer locations. For all harmonics, the unsteady loading noise is maximized along the rotor axis and minimized in the rotor plane, consistent with the dipole nature of loading noise. The solid blue line indicates the mean loading noise obtained from the indicial response method, and the solid red line corresponds to the quasi-steady approach. The dashed lines in each color mark the minimum and maximum SPLs from the PCE simulations, while the shaded regions highlight the range of output uncertainty introduced by variability in gust length. At the first harmonic ($m = 1$), SPL distributions at all observer locations remain centered around the mean, with comparable uncertainty between the unsteady and quasi-steady approaches. At

Table 6: Means and standard deviations of unsteady loading noise of the first five harmonics at $\theta = 0°$ (CV $= 0.10$) as a result of uncertainty in l_g.

Harmonic Index		$m = 1$	$m = 2$	$m = 3$	$m = 4$	$m = 5$
Quasi-Steady	Mean	36.57	41.57	43.34	43.22	41.46
	Std. Dev.	0.81	0.60	0.27	0.40	1.30
	Minimum	33.12	38.90	41.18	39.73	34.62
	Maximum	39.11	43.09	43.58	43.58	43.58
Unsteady	Mean	33.46	37.07	38.29	37.82	35.82
	Std. Dev.	0.83	0.61	0.26	0.37	1.33
	Minimum	29.64	33.48	36.53	35.15	27.68
	Maximum	36.01	38.60	38.52	38.16	37.98

higher BPFs, however, both approaches exhibit strong skewness at $m = 3$ and $m = 4$ and mild skewness at $m = 2$ and $m = 5$. In these cases, the mean SPLs are shifted toward the upper limit, indicating a higher probability of gust length producing noise closer to that bound. When the unsteady approach is applied, the mean SPLs are consistently lower than those obtained with the quasi-steady formulation. This reduction is linked to the decreased thrust magnitude under the unsteady model, as shown in Fig. 3(c), which in turn lowers the mean SPL in the UQ results. The largest decrease between the two approaches is observed at the 5$^{\text{th}}$ harmonic, although the overall SPL uncertainty remains comparable.

Furthermore, the largest SPL uncertainty occurs along the rotor axis, indicating that the acoustic magnitude at this location is particularly sensitive to unsteadiness in the aerodynamic loads. The mean, standard deviation, and minimum-to-maximum bounds of the output SPLs from the PCE simulations at $\theta = 0°$ are summarized in Table 6. The highest mean SPL is observed at $m = 3$ for both the quasi-steady and unsteady approaches, and both approaches also yield the smallest spread of data about the mean at this harmonic. In contrast, the widest spread occurs at $m = 5$, where the difference between the maximum and minimum values is larger for the unsteady approach. Although not shown, the variability decays beyond the fifth harmonic. It should be noted that these results are based on an input CV value of 0.10, corresponding to a standard deviation equal to 10% of the mean gust length. Although the outcome may vary depending on the choice of mean and standard deviation, our selections are based on reasonable and realistic considerations, as shown in Table 3. This suggests that, under most realistic conditions, the largest uncertainty is unlikely to occur at the first BPF or at very high harmonics. Instead, it is reasonable to state that the highest uncertainty tends to appear near the fifth harmonic.

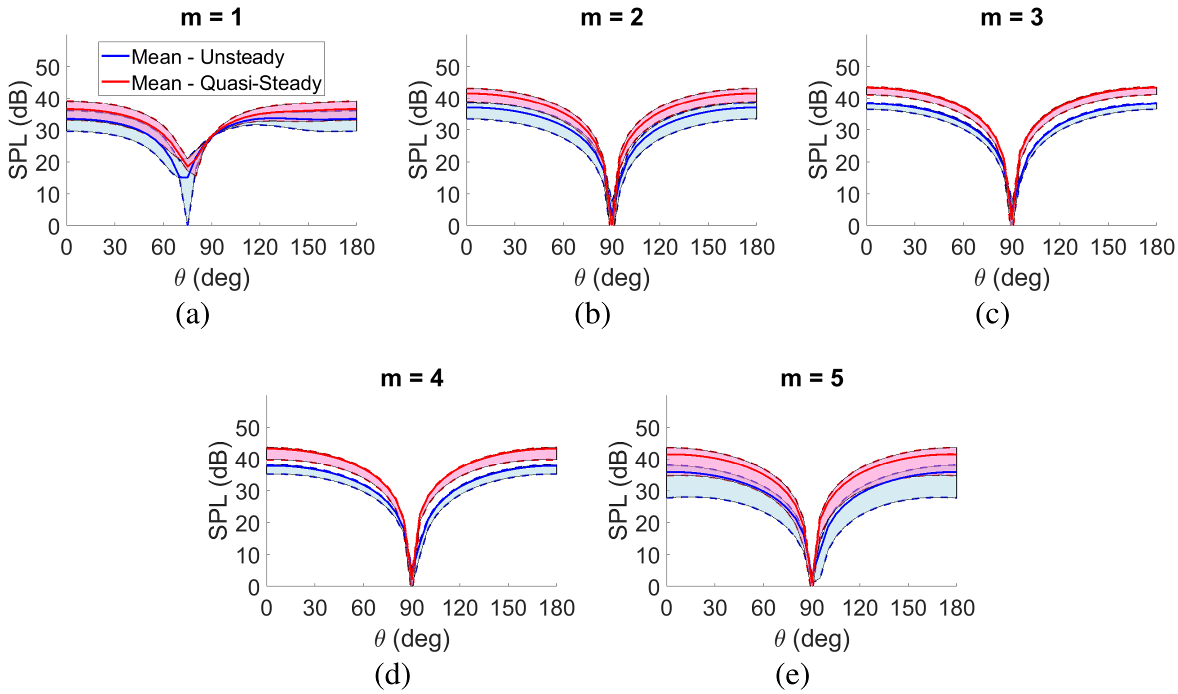

Fig. 7: Distribution of unsteady loading noise due to variations in gust length (l_g) at various observer locations (CV $= 0.10$): (a) 1st BPF noise, (b) 2nd BPF noise, (c) 3rd BPF noise, (d) 4th BPF noise, and (e) 5th BPF noise.

The distribution of output SPLs is further examined at $\theta = 0°$. Figure 8 presents histograms of SPLs for the first five BPFs together with fitted normal distribution curves. The same color scheme is applied: blue denotes the unsteady approach, and red denotes the quasi-steady approach. Both approaches exhibit approximately normal distributions at $m = 1$, with mild left skewness at $m = 2$ and $m = 5$, and strong left skewness at $m = 3$ and $m = 4$. Since the amplitudes of the harmonic loads that are responsible for the 3rd and 4th BPF noise do not vary significantly, the acoustic predictions are clustered near the upper region of the distribution, producing left skewness at $m = 3$ and $m = 4$. The PDFs obtained from the unsteady approach are shifted to the left relative to those from the quasi-steady approach due to the lower mean values. Nevertheless, the inclusion of unsteady aerodynamic effects does not alter the overall shape of the distributions.

Additional CV cases are studied to assess how the uncertainty of output SPLs responds to different levels of input variability. CV represents the amount of variation relative to the mean; for instance, a CV of 0.10 corresponds to a standard deviation equal to 10% of the mean. Figure 9 presents the linear-fit

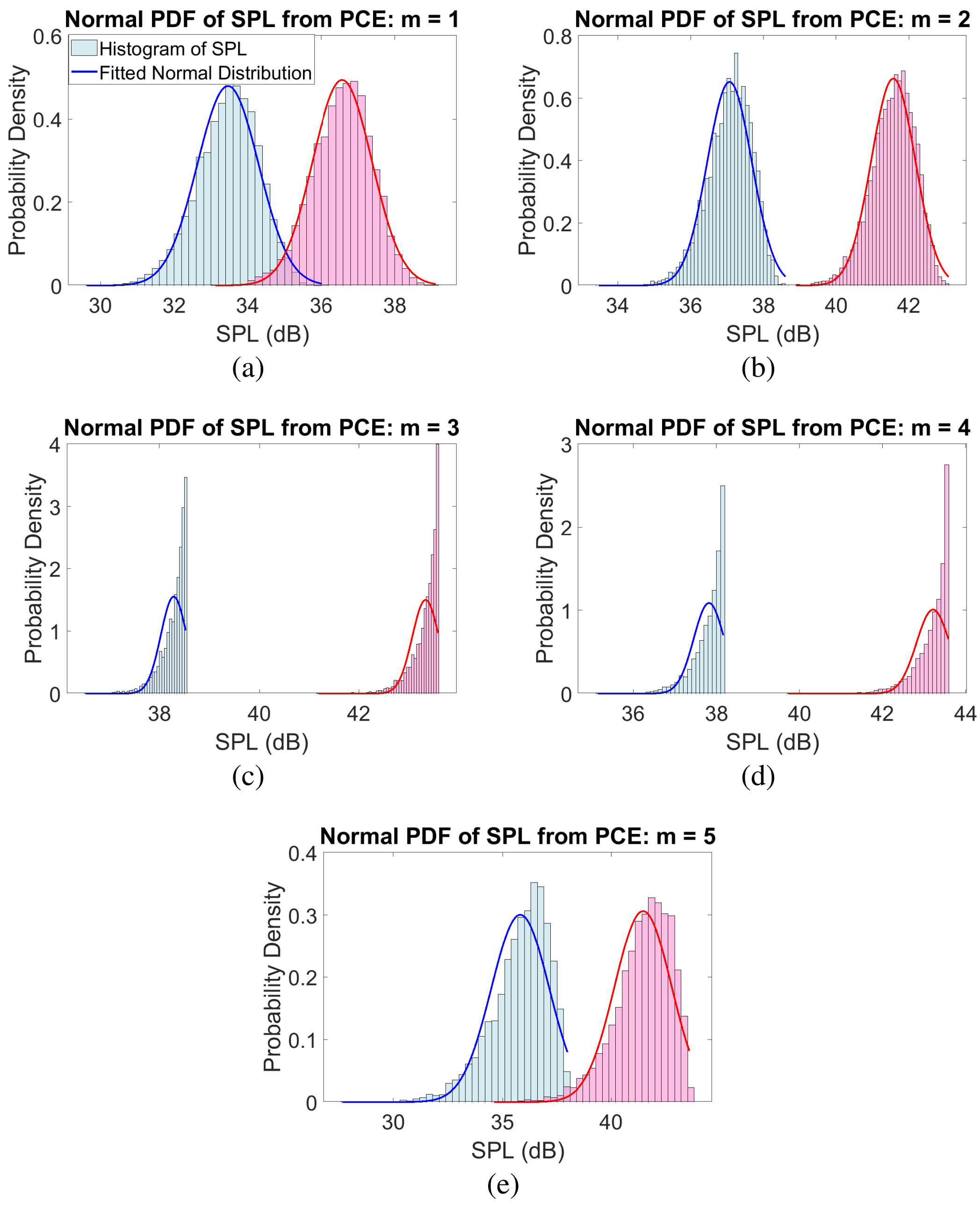

Fig. 8: Histogram and fitted normal PDF of the output SPLs at $\theta = 0°$ from PCE simulation as a result of uncertainty in gust length (CV $= 0.10$): (a) 1^{st} BPF noise, (b) 2^{nd} BPF noise, (c) 3^{rd} BPF noise, (d) 4^{th} BPF noise, and (e) 5^{th} BPF noise. Blue indicates acoustic data using the unsteady approach, and red indicates acoustic data using the quasi-steady approach.

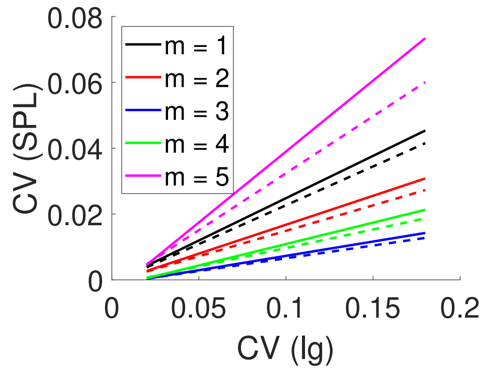

Fig. 9: Linear-fit relationship between the coefficient of variation of the output SPL and the coefficient of variation of the input gust length at $\theta = 0°$: quasi-steady approach in dashed line and unsteady approach in solid line.

relationship between the CVs of gust length and the CVs of SPL at $\theta = 0°$. The dashed line denotes the quasi-steady approach, while the solid lines denote the unsteady approach. For the quasi-steady approach, the increase in SPL variability with respect to gust length variability is most gradual at $m = 3$ and $m = 4$, with slopes of 0.0774 and 0.1125, respectively. This implies that a 0.1 increase in gust-length CV leads to only a 0.0077 increase in the CV of the 3^{rd} BPF loading noise and a 0.0113 increase in the CV of the 4^{th} BPF loading noise. By contrast, the slope at $m = 5$ is 0.3457, indicating a much steeper response. For example, when gust length varies between 0.1125 and 0.1375 m, the 5^{th} BPF unsteady loading noise corresponding to one standard deviation from the mean is 40.03–42.89 dB, while two standard deviations correspond to 38.59–44.33 dB. Thus, the 5^{th} harmonic consistently exhibits the highest rate of uncertainty growth, confirming that SPL uncertainty increases most rapidly at $m = 5$. The amplitude of the harmonic load related to the 5^{th} BPF noise fluctuated the most when the gust length was varied, thus producing the highest rate of uncertainty in the 5^{th} harmonic noise. A similar trend is observed for the unsteady approach. However, the CV values are consistently higher than those of the quasi-steady approach. Since the standard deviations remain comparable between the two models, the reduced mean SPL associated with the unsteady approach results in larger CV values.

Acoustic Impact due to Gust Amplitude Alone

Another gust characteristic that can induce unsteadiness in aerodynamic loads on a rotor disk is its amplitude. For this analysis, the gust length is fixed at its mean value. The directivity patterns in Fig.10

Table 7: Means and standard deviations of unsteady loading noise of the first five harmonics at $\theta = 0°$ (CV $= 0.10$) as a result of uncertainty in V_p.

Harmonic Index		$m = 1$	$m = 2$	$m = 3$	$m = 4$	$m = 5$
Quasi-Steady	Mean	36.60	41.58	43.37	43.30	41.63
	Std. Dev.	0.89	0.89	0.89	0.90	0.92
	Minimum	32.66	37.69	39.67	39.14	37.91
	Maximum	39.27	44.17	46.35	45.89	44.62
Unsteady	Mean	33.48	37.11	38.33	37.89	35.99
	Std. Dev.	0.91	0.90	0.91	0.90	0.91
	Minimum	29.75	33.30	34.80	33.80	32.31
	Maximum	36.16	40.13	40.84	40.31	38.71

remain consistent with those observed in the previous case involving uncertainty in gust length. The primary difference lies in the distribution of the output SPLs. As shown in Fig.10, the means of the output SPLs are generally centered within the distributions at all observer locations and all harmonics for both the unsteady and quasi-steady approaches. Notable differences appear at $m = 3$ and $m = 4$. In the gust-length case discussed previously, the distributions were left-skewed, with a higher concentration of data near the maximum values. In contrast, when gust amplitude is treated as the uncertain parameter, the distributions exhibit no skewness.

The SPL distribution at $\theta = 0°$ in Fig.11 further confirms the absence of skewness in the output data. The means, standard deviations, and minimum-to-maximum values for both unsteady and quasi-steady approaches are summarized in Table 7. The standard deviations remain relatively constant across all harmonic indices, with no differences observed between the two approaches. For both approaches, the smallest mean occurs at $m = 1$, while the largest mean occurs at $m = 3$. The difference between the maximum and minimum SPLs is also similar for both aerodynamic approaches. Thus, the inclusion of unsteady aerodynamic effects shifts the entire output distribution without altering its overall range.

The relationship between the input CV and the output CV for both aerodynamic approaches is shown in Fig. 12. For the quasi-steady approach, the output SPL CV exhibits a linear dependence on the input gust-amplitude CV at all harmonic indices. Across $m = 2$–5, the slopes are relatively constant at 0.22, whereas the slope at $m = 1$ is slightly higher at 0.26. This implies that for every 0.1 increase in gust-amplitude CV, the CV of the 1^{st} BPF noise increases by 0.026, while the CVs of the higher-harmonic noise increase by 0.022. Since the output SPLs follow normal distributions, these relationships can be

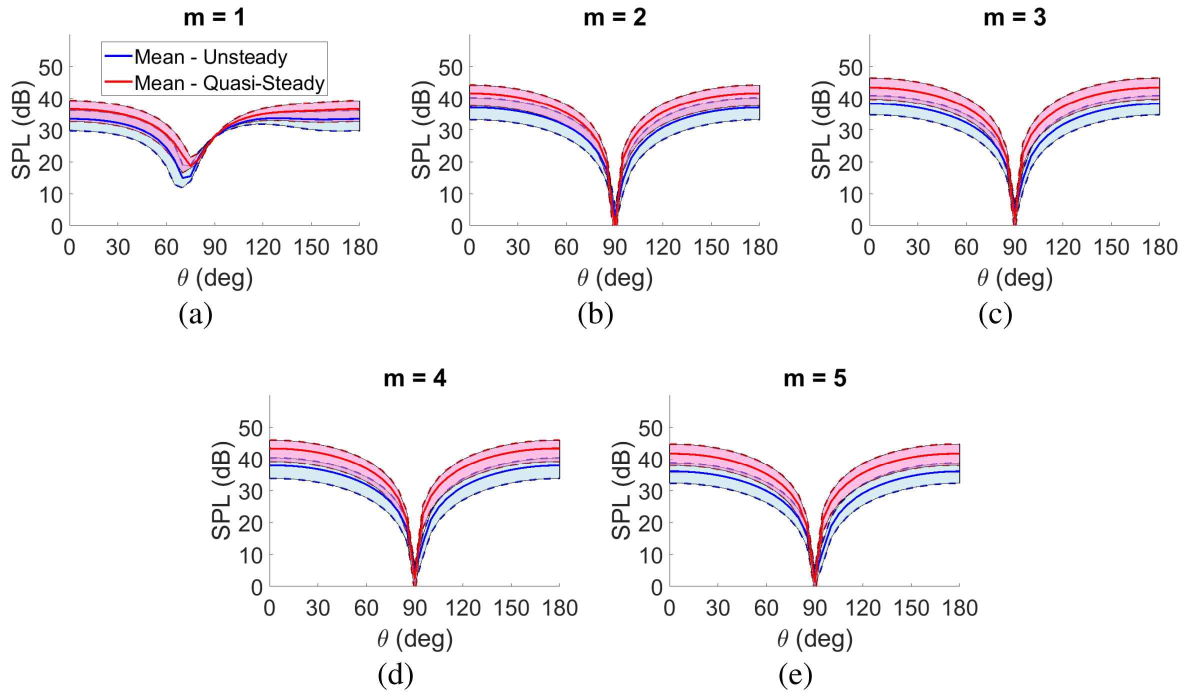

Fig. 10: Distribution of unsteady loading noise due to variations in gust amplitude (V_p) at various observer locations (CV $= 0.10$): (a) 1st BPF noise, (b) 2nd BPF noise, (c) 3rd BPF noise, (d) 4th BPF noise, and (e) 5th BPF noise.

used to quantify probabilistic bounds. For an input gust-amplitude CV of 0.10, there is a 95% probability that the 1st BPF noise lies between 34.70 and 38.50 dB. Under the same conditions, the corresponding 95% probability ranges are 39.75–43.41 dB for the 2nd BPF, 41.46–45.28 dB for the 3rd BPF, 41.39–45.21 dB for the 4th BPF, and 39.80–43.46 dB for the 5th BPF.

Since the mean values of the unsteady approach are reduced while the standard deviations remain unchanged across all harmonic indices (Table 7), the linear-fit relationship between gust-amplitude CV and SPL CV in Fig. 12 follows the same trend as the quasi-steady case but with steeper slopes. It is important to note that although the CV of the 1st harmonic SPL increases more rapidly, this does not imply greater absolute uncertainty of the output SPL, as the mean values differ among harmonic indices. Consequently, the relative distributions of SPLs with respect to their means are similar across all harmonics. A comparison between Fig.12 and Fig.9 further shows that gust-length variability produces greater uncertainty in the 5th harmonic SPL than gust-amplitude variability for both aerodynamic approaches. By contrast, the CVs of the 2nd–4th harmonic SPLs increase more rapidly with gust-amplitude CV than with gust-length CV,

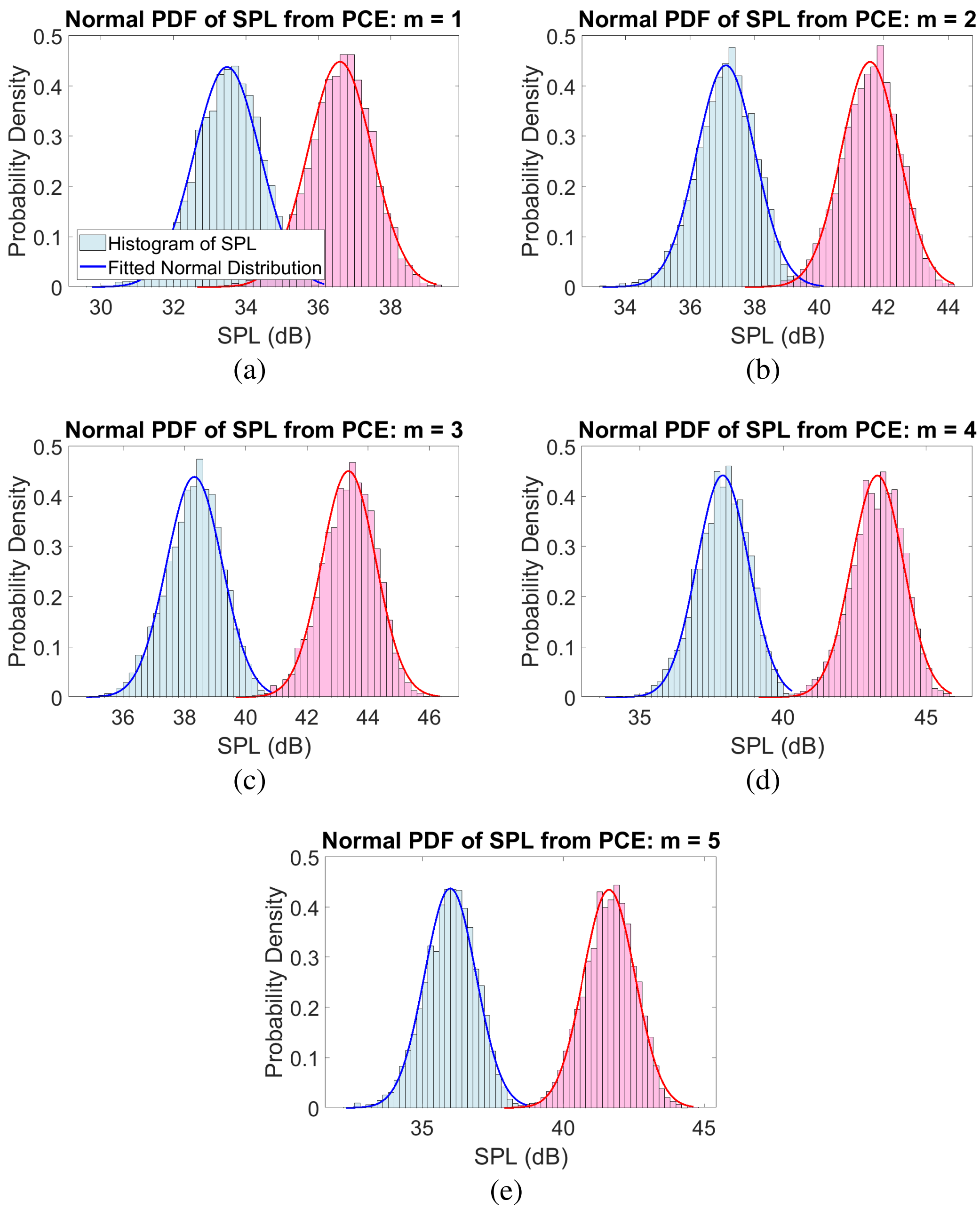

Fig. 11: Histogram and fitted normal PDF of the output SPLs at $\theta = 0°$ from PCE simulation as a result of uncertainty in gust amplitude (CV $= 0.10$): (a) 1st BPF noise, (b) 2nd BPF noise, (c) 3rd BPF noise, (d) 4th BPF noise, and (e) 5th BPF noise. Blue indicates acoustic data using the unsteady approach, and red indicates acoustic data using the quasi-steady approach.

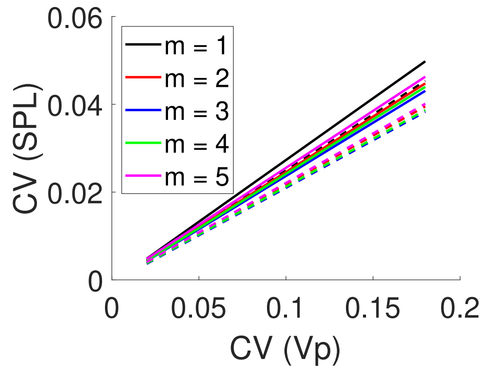

Fig. 12: Linear-fit relationship between the coefficient of variation of the output SPL and the coefficient of variation of the input gust peak velocity at $\theta = 0°$: quasi-steady approach in dashed line and unsteady approach in solid line.

indicating that the uncertainty in SPL at these harmonics is more sensitive to variations in gust amplitude.

Acoustic Impact due to Combined Gust Parameters

In this subsection, uncertainties in both gust length and amplitude are considered simultaneously. Figure 13 illustrates the resulting SPL uncertainty across observer locations between $0°$ and $180°$ for the two aerodynamic approaches. Consistent with the single-parameter UQ cases, the largest spread of unsteady loading noise occurs at the rotor axis for all harmonics. The output distributions at $m = 3$ and $m = 4$ resemble those from the gust-amplitude case, as the mean SPLs are not located near the maximum values. In comparison with the noise directivity uncertainty using the quasi-steady approach, the noise directivity uncertainty using the unsteady approach shifts down, and this shift is pronounced as the harmonic index increases. The distributions at $\theta = 0°$ are shown in Fig.14. In general, both unsteady and quasi-steady approaches follow the normal distributions at all harmonics. Table 8 shows means and standard deviations at all harmonics for each case. The minimum and maximum SPLs further indicate that the largest range of uncertainty occurs at $m = 5$, with values of 12.12 dB for the quasi-steady approach and 14.66 dB for the unsteady approach.

The relationship between the CV of output SPL and the CV of the combined input parameters is shown in Fig. 15 for an observer at $\theta = 0°$. Both input CVs of gust length and amplitude are jointly varied from 0.02 to 0.18. For the quasi-steady approach, the 5^{th} harmonic SPL exhibits the steepest

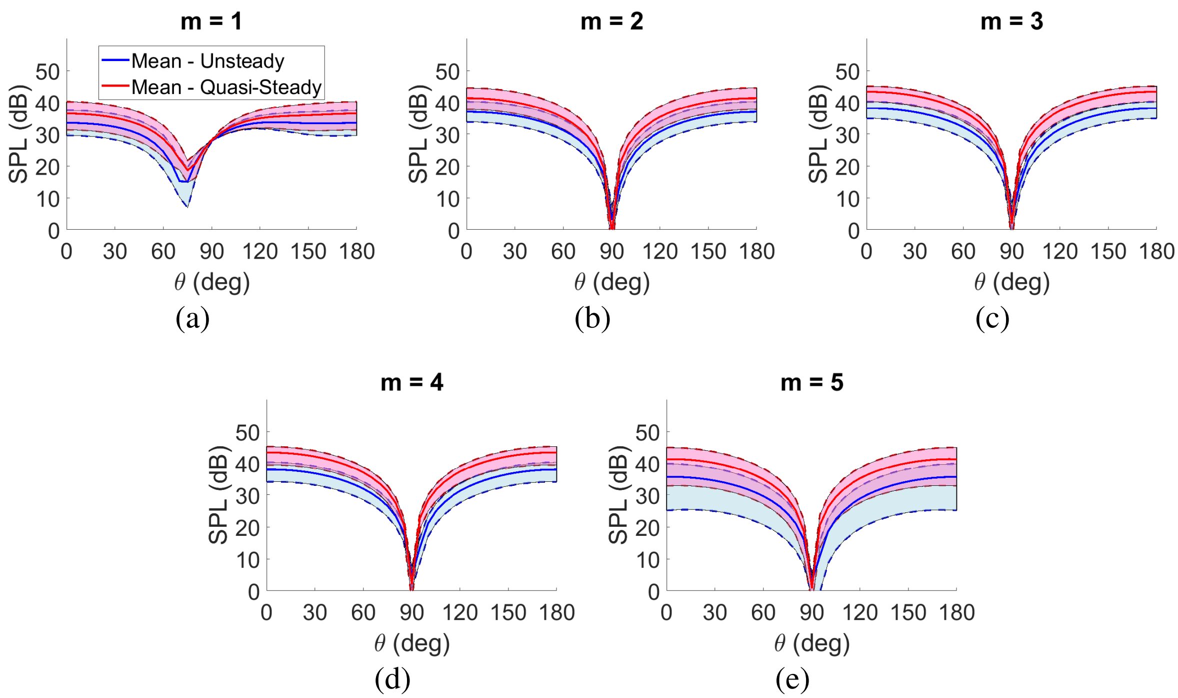

Fig. 13: Distribution of unsteady loading noise due to variations in gust length (l_g) and amplitude (V_p) at various observer locations (CV $= 0.10$): (a) 1^{st} BPF noise, (b) 2^{nd} BPF noise, (c) 3^{rd} BPF noise, (d) 4^{th} BPF noise, and (e) 5^{th} BPF noise.

Table 8: Means and standard deviations of unsteady loading noise of the first five harmonics at $\theta = 0°$ (CV $= 0.10$) as a result of uncertainty in V_p and l_g.

Harmonic Index		$m = 1$	$m = 2$	$m = 3$	$m = 4$	$m = 5$
Quasi-Steady	Mean	36.47	41.36	43.36	43.39	41.31
	Std. Dev.	1.15	1.11	0.84	0.88	1.54
	Minimum	31.34	37.79	40.23	39.48	32.83
	Maximum	40.22	44.53	45.07	45.24	44.95
Unsteady	Mean	33.51	37.00	38.18	37.96	35.65
	Std. Dev.	1.17	1.03	0.92	0.92	1.75
	Minimum	29.54	33.86	34.97	34.14	25.17
	Maximum	37.45	40.20	40.25	40.30	39.83

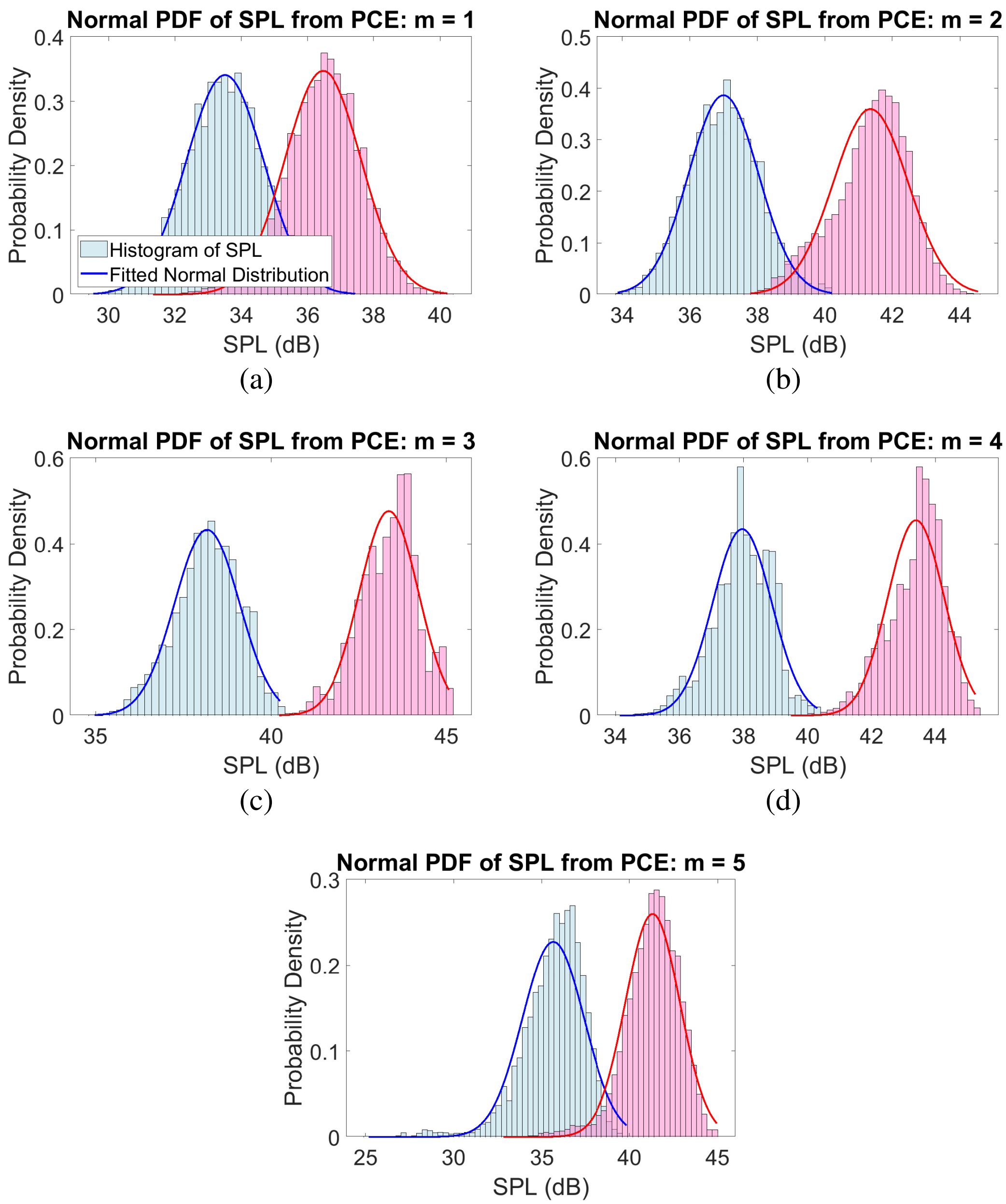

Fig. 14: Histogram and fitted normal PDF of the output SPLs at $\theta = 0^\circ$ from PCE simulation as a result of uncertainty in gust length and amplitude (CV $= 0.10$): (a) 1^{st} BPF noise, (b) 2^{nd} BPF noise, (c) 3^{rd} BPF noise, (d) 4^{th} BPF noise, and (e) 5^{th} BPF noise. Blue indicates acoustic data using the unsteady approach, and red indicates acoustic data using the quasi-steady approach.

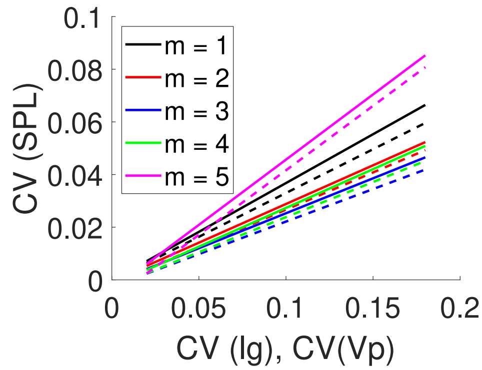

Fig. 15: Linear-fit relationship between the coefficient of variation of the output SPL and the coefficient of variation of the input gust length and gust amplitude at $\theta = 0°$: quasi-steady approach in dashed line and unsteady approach in solid line.

growth (linear-fit slope of 0.49) as the input CVs increase, followed by the 1st harmonic (slope of 0.33). Since the output SPL distributions are normal, introducing uncertainties to the input parameters with standard deviations equal to 10% of their mean yields a 95% probability (± 2 standard deviation from the mean) that the resulting 5th harmonic noise lies between 37.26 and 45.36 dB, and the 1st harmonic noise lies between 34.06 and 38.88 dB. Comparison of the quasi-steady results in Fig.15 with those in Figs. 9 and 12 indicates that gust-length variability contributes more strongly to the uncertainty of the 5th harmonic noise than gust-amplitude variability. In contrast, the uncertainties of the 2nd–4th harmonic noise are more sensitive to gust-amplitude variability, with trends resembling those in Fig. 12. The same conclusions apply to the unsteady approach, though the slopes of SPL CVs are consistently higher than in the quasi-steady case due to the reduction in mean SPL under unsteady conditions.

The boxplots in Fig.16 and Fig.17 illustrate the distribution of output SPLs at $\theta = 0°$ for CV $= 0.10$ using the quasi-steady and unsteady approaches, respectively. The upper and lower dashed lines extending from each blue box (whiskers) represent the top and bottom 25% of the data, while the box itself contains the central 50% of the data, with the red horizontal line marking the median. Red plus signs denote outliers. For the quasi-steady approach (Fig. 16), the widest distributions occur at $m = 1$ and $m = 5$, as indicated by the long whiskers. The 1st harmonic data are concentrated near 36 dB, while the 5th harmonic data cluster near 42 dB, and both harmonics also exhibit the largest number of outliers. By contrast, the 2nd harmonic is concentrated near 42 dB but shows shorter whiskers, indicating a narrower spread. At $m = 3$ and $m = 4$, the medians are the highest among all harmonics, but the corresponding variations in

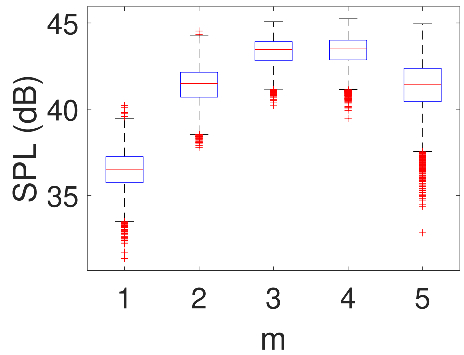

Fig. 16: Boxplots of the output SPLs for the first five BPFs at $\theta = 0°$ using the quasi-steady approach (CV $= 0.10$).

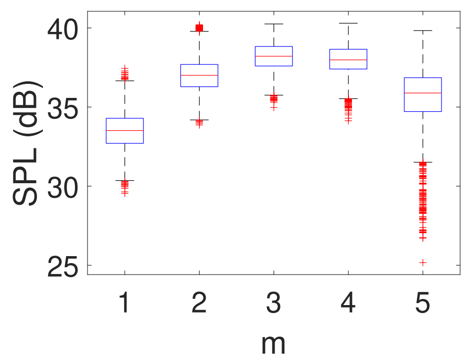

Fig. 17: Boxplots of the output SPLs for the first five BPFs at $\theta = 0°$ using the unsteady approach (CV $= 0.10$).

acoustic magnitude remain small, reflecting limited sensitivity to the combined input uncertainties.

The boxplot in Fig.17 shows that when unsteady aerodynamic effects are included, the distributions of the five harmonic SPLs are generally similar to those of the quasi-steady case in Fig.16, but with reduced mean values. The interquartile range (IQR), defined as the height of the blue box containing 50% of the data, exhibits only minor differences between the two aerodynamic approaches, as summarized in Table 9. The largest difference in IQR occurs at $m = 5$, where 50% of the noise data generated by the combined variability of gust length and amplitude falls within approximately 2 dB in both the quasi-steady and unsteady approaches.

Table 9: Comparison of the IQRs between quasi-steady and unsteady approaches.

Approaches	$m = 1$	$m = 2$	$m = 3$	$m = 4$	$m = 5$
Quasi-Steady	1.5095	1.4438	1.1048	1.1491	1.9309
Unsteady	1.5846	1.4075	1.2354	1.2523	2.1403

The outliers in Figs. 16 and 17 represent the extreme ends of the data. To identify the combinations of input parameters that contribute to these extreme SPLs, parallel coordinate plots (PCPs) are employed. PCPs provide a means of visualizing the relationships between multiple input parameters and output responses, enabling the identification of parameter combinations that generate outliers [36]. Figure 18 presents PCPs for all five harmonics at $\theta = 0°$ using the unsteady approach. The first two vertical axes correspond to the input parameters—gust amplitude (V_p) in m/s and gust length (l_g) in m—while the third axis shows the resulting SPLs in dB. Gray lines represent all parameter combinations leading to SPL outcomes, and the red lines highlight those associated with SPL outliers identified in Fig. 17. Tracing these red lines reveals the specific input conditions that generate outliers. The lower outliers of the 1^{st}–3^{rd} harmonics arise from low values of both V_p and l_g. In particular, combinations of V_p and l_g below their respective means (0.6441 m/s and 0.125 m) produce these extreme values. Conversely, upper outliers in the 1^{st} and 2^{nd} harmonics occur when both V_p and l_g exceed their mean values. At the 4^{th} harmonic, however, lower SPL outliers result from combinations of below-mean V_p with above-mean l_g. At the 5^{th} harmonic, lower outliers are observed even at higher V_p, indicating that large gust amplitudes do not always yield strong unsteady loading noise when paired with longer gust lengths.

To further illustrate the combinations of input parameters that lead to low unsteady loading noise, the lowest 20% of the output SPLs are traced back to their corresponding inputs. In Fig. 19, the gray lines represent all parameter combinations, while the red lines highlight those associated with the lowest 20% of SPLs. For the first three harmonics, low noise is generated when a low gust amplitude is combined with a narrow gust length. At higher harmonics ($m = 4$ and $m = 5$), however, low noise results from the combination of low gust amplitude with a wider gust length. Conversely, these results indicate that longer gust lengths contribute to higher unsteady loading noise at low harmonics ($m = 1$–3), whereas shorter gust lengths amplify noise production at higher harmonics ($m = 4$–5) as expected.

Conclusions

This study developed and demonstrated a PCE–based uncertainty quantification framework to assess unsteady loading noise of a hovering rotor subjected to vertical gust disturbances. By coupling a frequency-domain loading noise model with quasi-steady BEMT and unsteady aerodynamic formula-

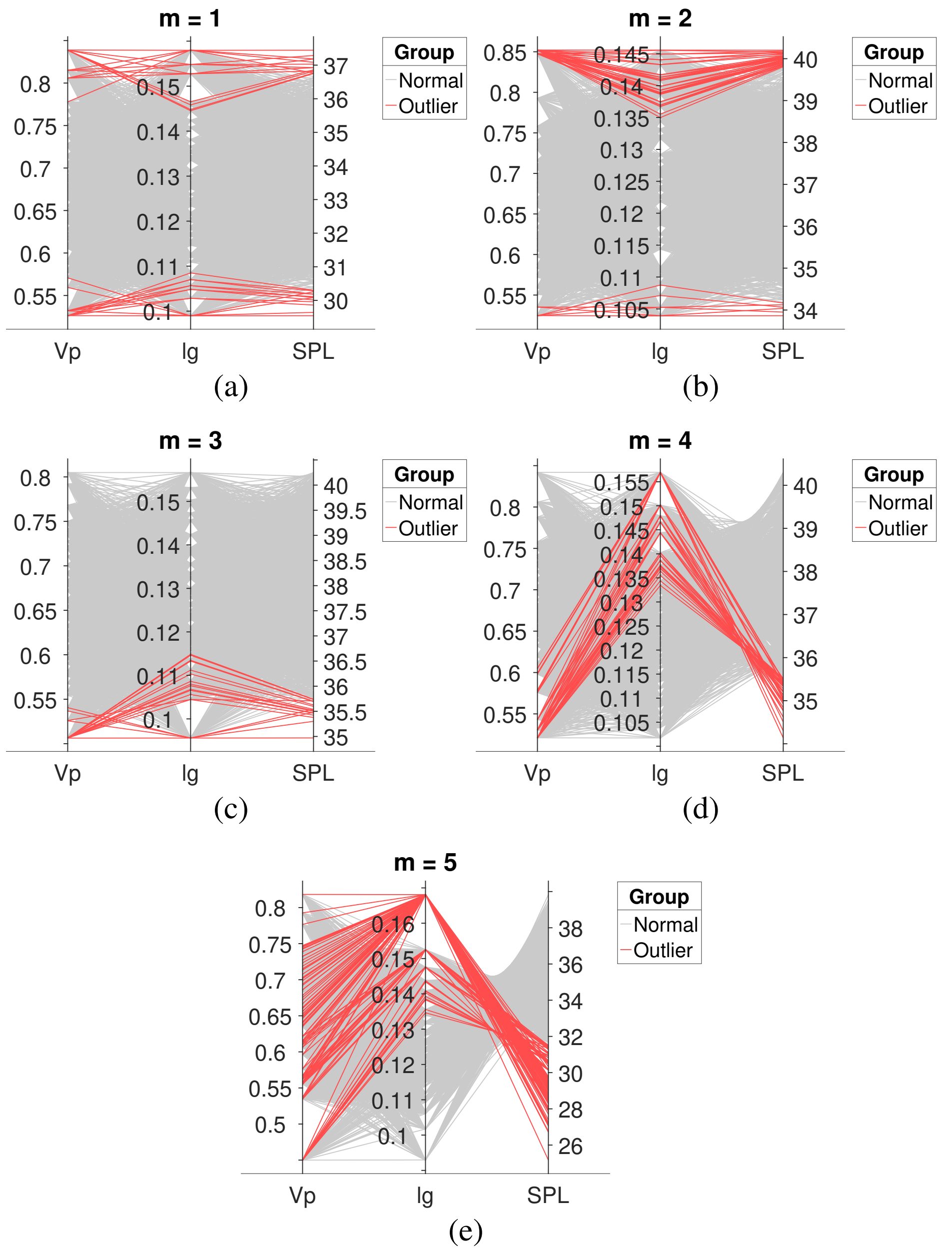

Fig. 18: Parallel coordinate plots of two input parameters (V_p and l_g) and one output parameter (SPL at $\theta = 0°$): (a) 1$^{\text{st}}$ BPF noise, (b) 2$^{\text{nd}}$ BPF noise, (c) 3$^{\text{rd}}$ BPF noise, (d) 4$^{\text{th}}$ BPF noise, and (e) 5$^{\text{th}}$ BPF noise.

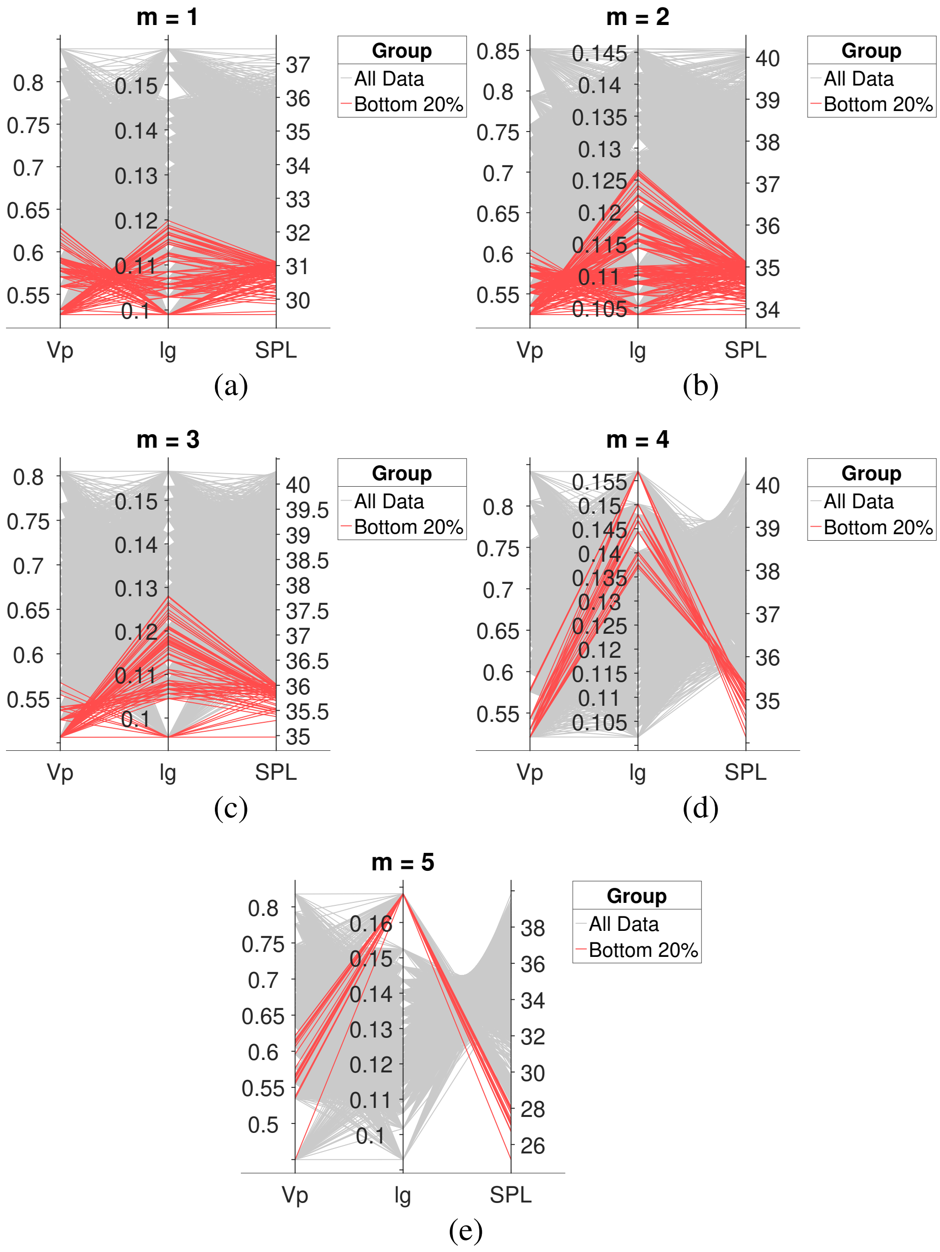

Fig. 19: Parallel coordinate plots of the combinations of V_p and l_g that lead to the lowest 20% of the output SPLs at $\theta = 0°$: (a) 1st BPF noise, (b) 2nd BPF noise, (c) 3rd BPF noise, (d) 4th BPF noise, and (e) 5th BPF noise.

tions, the approach efficiently captured the propagation of gust-induced inflow uncertainties into acoustic responses. Validation against Monte Carlo simulations confirmed that the PCE method accurately reproduces both the mean trends and statistical bounds of sound pressure levels while requiring an order of magnitude fewer simulations, making it well suited for rapid aeroacoustic uncertainty analyses.

The results show that unsteady loading noise uncertainty is consistently maximized along the rotor axis, reflecting the dipole-like directivity of loading noise. Among the gust parameters considered, gust length plays a dominant role in driving acoustic uncertainty at higher blade-passing frequency harmonics, particularly near the fifth harmonic, whereas gust amplitude more strongly influences uncertainty at lower and mid harmonics. These findings indicate that the largest acoustic uncertainty does not necessarily occur at the first blade-passing frequency, but rather at intermediate harmonics under realistic gust conditions.

Incorporating unsteady aerodynamic effects through the indicial response method reduces the mean sound pressure levels at all harmonics compared to the quasi-steady formulation. However, the overall magnitude and structure of the uncertainty bounds remain largely unchanged, indicating that unsteady aerodynamics primarily shift the acoustic response rather than fundamentally altering its sensitivity to inflow variability. Finally, the use of parallel coordinate plots provided clear insight into the combinations of gust parameters responsible for extreme noise outcomes. Overall, the proposed framework offers an efficient and physically interpretable tool for evaluating rotor noise robustness and supports uncertainty-aware noise-reduction strategies for advanced air mobility and eVTOL rotor designs.

Appendix

Figure A.1 presents the directivity of unsteady loading noise up to the 15^{th} harmonic, with gray shaded regions indicating the uncertainty bounds. The red dashed lines denote the mean SPL as a function of observer angle. At $\theta = 0°$, the mean SPL reaches its maximum at the $m = 3$ harmonic and subsequently decays at higher harmonics. In addition, the associated uncertainty decreases beyond $m = 5$.

References

[1]Greenwood, E., Brentner, K. S., Rau, R. F., and Gan, Z. F. T., "Challenges and Opportunities for Low Noise Electric Aircraft," *International Journal of Aeroacoustics*, 21, (5–7), 2022, 315–381, DOI: 10.1177/1475472X221107377

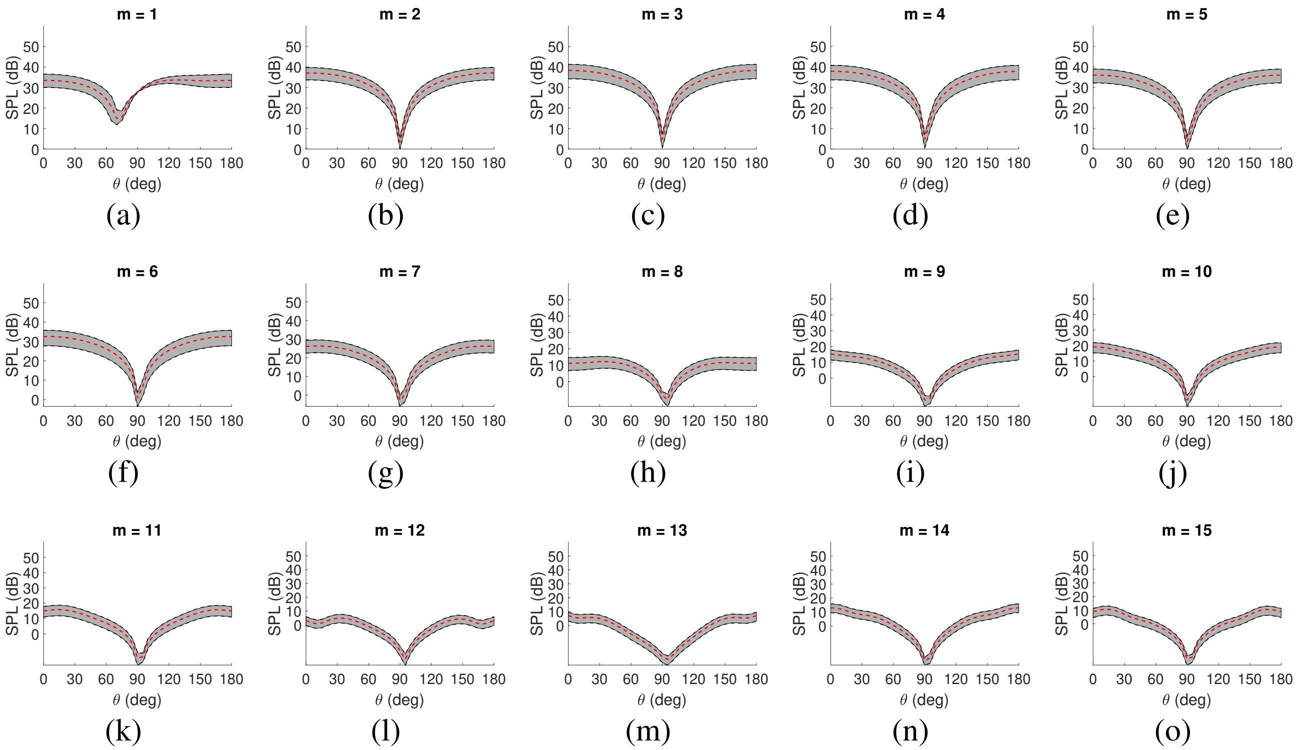

Fig. A.1: Uncertainty directivity plots of unsteady loading noise up to 15^{th} harmonics as a result of varying the gust amplitude (V_p).

[2]Hua, Y. and Mankbadi, R., "Prediction and Control of Broadband Noise Associated with Advanced Air Mobility—A Review," *Applied Sciences*, 14, (18), 2024, 8455, DOI: 10.3390/app14188455

[3]Li, S. and Lee, S., "Analytic Prediction of Rotor Broadband Noise with Serrated Trailing Edges with Applications to Urban Air Mobility Aircraft," *Journal of the American Helicopter Society*, 69, (3), 2024, 032005, DOI: 10.4050/JAHS.69.032005

[4]Weitsman, D. and Greenwood, E., "Passive Blade–Vortex Interaction Noise Reduction Using Embedded In-Blade Resonator Cavities," *AIAA Journal*, 63, (12), 2025, 5313–5325, DOI: 10.2514/1.J064772

[5]Won, J. and Lee, S., "Rotor Noise Reduction Using Beveled Trailing Edges and Hybrid," AIAA SciTech Forum Proceedings, Orlando, FL, January 12–16, 2026.

[6]Jia, Z. and Lee, S., "Computational Study on Noise of Urban Air Mobility Quadrotor Aircraft," *Journal of the American Helicopter Society*, 67, 2022, 012009, DOI: 10.4050/JAHS.67.012009

[7]Jia, Z. and Lee, S., "High-Fidelity Computational Analysis on the Noise of a Side-by-Side Hybrid VTOL Aircraft," *Journal of American Helicopter Society*, 67, (2), 2022, 1–14, DOI:

10.4050/JAHS.67.022005

[8]Gardner, A. D., Kostek, A. A., Lößle, F., and Braukmann, J. N., "Experiments and Modeling of a Single Multicopter Rotor Response to Sinusoidal Vertical Gusts," *Journal of the American Helicopter Society*, 70, (3), 2025, 032002, DOI: 10.4050/JAHS.70.032002

[9]Feinerman, J. A., Koushik, S., and Schmitz, F. H., "Effect of Leading-Edge Serrations on Helicopter Blade-Vortex Interaction Noise," *Journal of the American Helicopter Society*, 62, (3), 2017, 1–11, DOI: 10.4050/JAHS.62.032001

[10]Li, Q., Wang, L., and Zhang, R., "Effect of Rotation Speed Fluctuation on Rotor Noise generation: A Numerical and Experimental Study," *Journal of Sound and Vibration*, 595, 2024, 118717, DOI: 10.1016/j.jsv.2024.118717

[11]Kvurt, A. and Stalnov, O., "From the Blade Geometry to Prediction of Tonal Noise Component in Hover," Paper AIAA 2022–3076, 28th AIAA/CEAS Aeroacoustics Conference Proceedings, Southampton, UK, June 14–17, 2022, DOI: 10.2514/6.2022-3076

[12]Gill, H. and Lee, S., "Prediction of Rotor Unsteady Loading Noise in Hover Using an Unsteady Blade Element Momentum Theory," Paper AIAA 2025–1043, AIAA SciTech Forum Proceedings, Orlando, FL, January 6–10, 2025, DOI: 10.2514/6.2025-1043

[13]Shao, M., He, L., McFarland, D. M., Jiang, H., and Chen, S., "Numerical Investigation of Pitching Airfoil Subjected to Incoming Gust," *Physics of Fluids*, 37, (5), 2025, 056101, DOI: 10.1063/5.0266004

[14]Xiu, D. and Karniadakis, G. E., "The Wiener–Askey Polynomial Chaos for Stochastic Differential Equations," *SIAM Journal on Scientific Computing*, 24, (2), 2003, 619–644, DOI: 10.1137/S1064827501387826

[15]Ricks, A., Kingan, M. J., and Glegg, S. A. L., "Uncertainty Quantification for the Aeroacoustics of Rotating Blades in the Time Domain," *Applied Acoustics*, 139, 2018, 57–68, DOI: 10.1016/j.apacoust.2018.04.012

[16]Kha, J., Croaker, P., Karimi, M., and Skvortsov, A., "Uncertainty Analysis in Airfoil–Turbulence Interaction Noise Using Polynomial Chaos Expansion," *AIAA Journal*, 62, (2), 2024, 412–426, DOI: 10.2514/1.J062941

[17]Radotich, M., "Conceptual Design of Tiltrotor Aircraft for Urban Air Mobility," Aeromechanics for Advanced Vertical Flight Technical Meeting Proceedings, San Jose, CA, Jan. 25–27, 2022.

[18]Sagaga, J. and Lee, S., "High-Fidelity Computational Study of Aerodynamic Noise of Side-by-Side Rotor in Full Configuration," *Journal of Sound and Vibration*, 592, 2024, 118607, DOI: 10.1016/j.jsv.2024.118607

[19]Leishman, J. G., "Subsonic Unsteady Aerodynamics Caused by Gusts Using the Indicial Method," *Journal of Aircraft*, 33, (5), 1996, 828–835, DOI: 10.2514/3.47029

[20]Goldstein, M., "Unified Approach to Aerodynamic Sound Generation in the Presence of Solid Boundaries," *Journal of the Acoustical Society of America*, 56, (2), 1974, 497–509, DOI: 10.1121/1.1903283

[21]Sarojini, D., Chambers, J. T., Wolfe, L., Doring, R., Despins, R., Ruh, M. L., Yan, J., Orndorff, N., Scotzniovsky, L., Xiang, R., Zhao, H., Krokowski, J. J., Chen, J.-S., Joseph, C., Anderson, R. M., Ning, A., Gill, H., Lee, S., Cheng, Z., Cao, Z., Mi, C., Cronk, A., Guibert, A., Kim, A., Meng, S., Silva, C., and Hwang, J. T., "Review of Computational Models for Large-Scale MDAO of Urban Air Mobility Concepts," Paper AIAA 2024-0377, AIAA SciTech Forum Proceedings, Orlando, FL, January 8–12, 2024, DOI: 10.2514/6.2024-0377

[22]van Schie, S., Ruh, M., Fletcher, A., Warner, M., Sperry, M., Scotzniovsky, L., Orndorff, N., Xiang, R., Yan, J., Zhao, H., Krokowski, J., Chen, J., Sarojini, D., Gill, H., Lee, S., Tagg, A., Anderson, R., Green, E., Joseph, C., Ning, A., Cheng, Z., Cao, Z., Mi, C., Guibert, A., Cronk, A., Kim, A., Meng, S., Silva, C., and Hwang, J., "Large-Scale Distributed Multidisciplinary Design Optimization of the NASA Lift-Plus-Cruise Air Taxi Concept," Paper AIAA 2025-0362, AIAA SciTech Forum Proceedings, Orlando, FL, January 6–10, 2025, DOI: 10.2514/6.2025-0362

[23]Guttin, L., "On the Sound Field of a rotating Propeller," Technical Report NACA–TM–1195, National Advisory Committee for Aeronautics, October, 1948.

[24]Barry, F. W. and Magliozzi, B., "Noise Detectability Prediction Method for Low Tip Speed Propellers," Technical Report AFAPL–TR–71–37, Air Force Aero Propulsion Laboratory, June 1971.

[25]Hanson, D. B., "Influence of Propeller Design Parameters on Far-Field Harmonic Noise in Forward Flight," *AIAA Journal*, 18, (11), 1980, 1313–1319, DOI: 10.2514/3.50887

[26]Lowson, M. V. and Ollerhead, J. B., "A Theoretical Study of Helicopter Rotor Noise," *Journal of Sound and Vibration*, 9, (2), 1969, 197–222, DOI: 10.1016/0022-460X(69)90028-5

[27]Wright, S. E., "Sound Radiation from a Lifting Rotor Generated by Asymmetric Disk Loading," *Journal of Sound and Vibration*, 9, (2), 1969, 223–240, DOI: 10.1016/0022-460X(69)90029-7

[28]Gill, H., Lee, S., Ruh, M., and Hwang, J. T., "Applicability of Low-Fidelity Tonal and Broadband Noise Models on Small-Scale Rotors," Paper AIAA 2023–1547, AIAA SciTech Forum Proceedings, National Harbor, MD, January 23–27, 2023, DOI: 10.2514/6.2023-1547

[29]Brown, D. and Ollerhead, J. B., "Propeller Noise at Low Tip Speeds," Technical Report AFAPL–TR–71–55, Air Force Aero Propulsion Laboratory, September 1971.

[30]Whelchel, J., Alexander, W. N., and Intaratep, N., "Propeller Noise in Confined Anechoic and Open Environments," Paper AIAA 2020–1252, AIAA SciTech Forum Proceedings, Orlando, FL, January 6–10, 2020, DOI: 10.2514/6.2020-1252

[31]Leishman, J. G., *Principles of Helicopter Aerodynamics,*, Cambridge University Press, New York, second edition, 2006.

[32]Wagner, H., "Über die Entstehung des dynamischen Auftriebes von Tragflügeln," *Journal of Applied Mathematics and Mechanics*, 5, (1), 1925, 17–35, DOI: 10.1002/zamm.19250050103

[33]Wang, B., Warner, M., Tian, A., Scotzniovsky, L., and Hwang, J. T., "A Comparative Study of Uncertainty Quantification Methods in Gust Response Analysis of Lift-Plus-Cruise eVTOL Aircraft Wing," *arXiv*, January, 2025, DOI: 10.48550/arXiv.2501.03964

[34]Arnhem, N., Vries, R., Sinnige, T., Vos, R., Eitelberg, G., and Veldhuis, L. L. M., "Engineering Method to Estimate the Blade Loading of Propellers in Nonuniform Flow," *AIAA Journal*, 58, (12), 2020, 5332–5346, DOI: 10.2514/1.J059485

[35]Gill, H. and Lee, S., "Uncertainty Quantification of Unsteady Loading Noise of a Hovering Rotor Using Polynomial Chaos Expansion," Vertical Flight Society 81st Annual Forum Proceedings, Virginia Beach, VA, May 20–22, 2025, DOI: 10.4050/F-0081-2025-0060

[36]Khurana, M. and Yeo, H., "Uncertainty Quantification of the ONERA 7A Rotor Performance and Spanwise Structural Loads Using a Surrogate-Based Approach," *CEAS Acoustical Journal*, 15, 2024, 933–956, DOI: 10.1007/s13272-024-00768-0

List of Figures

List of Tables